# Monitoring Reinforced Concrete Cracking Behavior under Uniaxial Tension Using Distributed Fiber-Optic Sensing Technology

Han Liu, S.M.ASCE[1]; Shenghan Zhang[2]; Abdoul A. S. Coulibaly[3]; Jeffrey Cheng[4]; and Matthew J. DeJong, A.M.ASCE[5]

**Abstract:** Fiber-optic sensing (FOS) provides distributed strain measurement that can enhance both structural health monitoring (SHM) and laboratory testing capabilities. In particular, optical frequency domain reflectometry (OFDR) provides strain or temperature measurements every millimeter over tens of meters of fiber, with a high sampling rate. For RC applications with embedded fiber-optic cables, the sensitivity of the fibers and their ability to measure and survive cracking are both important considerations. In this study, tests were conducted on six RC specimens to investigate the effectiveness of using OFDR strain sensing to evaluate the cracking behavior of concrete and the deformation of steel reinforcing bars. Six types of fiber-optic cables with very different structures, sensitivity, and survivability were tested. Fibers were placed in the concrete and in grooves in the reinforcing bars. A new deconvolution method was developed; using the method, crack widths were accurately measured up to the target load levels using both the more sensitive fiber-optic cables and cables with reduced sensitivity but better survivability. OFDR strain sensing, combined with new methods of data processing, was shown to be capable of detecting distributed microcracking and providing reliable crack widths. The OFDR technique was also used to reveal the location-dependent bond-slip relationships between the concrete and rebar at early stages. **DOI: 10.1061/(ASCE)ST.1943-541X.0003191.** *© 2021 American Society of Civil Engineers.*

**Author keywords:** Distributed fiber optic sensing; Reinforced concrete; Crack width measurements; Bond-slip; OFDR; Sensitivity and survivability.

## Introduction

As many RC structures approach the end of their service life, there is a rising need for early detection and evaluation of damage in infrastructure; structural health monitoring (SHM) provides a potential solution (Brault and Hoult 2019b). Traditional SHM systems, such as strain gauges, accelerometers, linear variable differential transformers (LVDTs), and so forth, provide important information about structural behavior but only at a limited number of discrete points; this can limit the ability of these systems to detect damage when the damage location is not known a priori.

Distributed fiber-optic sensing (DFOS) and full field digital image correlation (DIC), however, can provide measurements at thousands of closely spaced points with minimal disruption to the mechanical behavior of structures. Optical frequency domain reflectometry (OFDR) is a special fiber-optic sensing (FOS) technology that uses Rayleigh scattering to obtain sub-millimeter-resolution measurements of strain or temperature dynamically over tens of meters (Barrias et al. 2016), while optical time domain reflectometry (OTDR) allows measurements over tens of kilometers with a resolution of about one meter (Haefliger et al. 2017). DFOS can also be used with standard fiber-optic cables, requires minimal maintenance costs, and provides a very stable sensing solution.

Recent research has shown the promising potential of evaluating the internal damage of RC structures using OFDR. Poldon et al. (2019) showed that Rayleigh backscattering can provide a better understanding of the shear behavior of RC through accurate measurements of tensile elongations and beam deflections. Haefliger et al. (2017) tested two reinforced concrete panels under diagonal tension with complex crack patterns to assess the combined application of DIC and FOS measurements. They found that the measurements of crack location and opening for both measurement techniques aligned accurately. Brault and Hoult (2019a) proposed three methods to calculate crack widths using the FOS strains measured by a nylon-coated fiber-optic cable. Brault et al. (2019) investigated the use of OFDR to monitor distributed strain, distributed deflections, and crack widths simultaneously for three beams in an RC building. A practical application of FOS to monitor the performance of bonds and the damage of RC beams in the postyield range of steel reinforcement was reported by Malek et al. (2019). Davis et al. (2017) conducted a series of tension tests on bare reinforcing bars and RC specimens to investigate shrinkage and the effect of tension stiffening. Other recent studies have also presented interesting results, including Rodríguez et al. (2015), Barrias et al. (2018), Villalba and Casas (2013), and Mata-Falcón et al. (2020).

[1]Graduate Research Assistant, Dept. of Civil and Environmental Engineering, Univ. of California, Berkeley, CA 94720. ORCID: https://orcid.org/0000-0002-8500-0610. Email: han_liu@berkeley.edu

[2]Postdoctoral Researcher, Dept. of Civil and Environmental Engineering, Univ. of California, Berkeley, CA 94720. Email: shenghan.zhang@berkeley.edu

[3]Graduate Research Assistant, Dept. of Civil and Environmental Engineering, Univ. of California, Berkeley, CA 94720. ORCID: https://orcid.org/0000-0002-5908-9594. Email: aascoulibaly20@berkeley.edu

[4]Undergraduate Research Assistant, Dept. of Civil and Environmental Engineering, Univ. of California, Berkeley, CA 94720. Email: jeffreycheng@berkeley.edu

[5]Associate Professor, Dept. of Civil and Environmental Engineering, Univ. of California, Berkeley, CA 94720 (corresponding author). ORCID: https://orcid.org/0000-0002-6195-839X. Email: dejong@berkeley.edu

Note. This manuscript was submitted on February 3, 2021; approved on July 22, 2021; published online on September 28, 2021. Discussion period open until February 28, 2022; separate discussions must be submitted for individual papers. This paper is part of the ***Journal of Structural Engineering***, © ASCE, ISSN 0733-9445.

Despite the aforementioned efforts, employing distributed FOS to monitor RC behavior in the field is still challenging for many reasons, including the typical contradiction between the durability and sensitivity of fiber-optic cables. When the coating and the core of a fiber-optic cable are not well bonded, the strain in the coating is transferred through shear, and the lack of friction can result in localized slipping during loading (Malek et al. 2019). Consequently, the width of the peaks in the FOS strain profile can be affected by (1) debonding of the optical fiber from the concrete on either side of the crack, (2) deformation of the fiber coating, and (3) slip between the fiber layers. Therefore, each type of fiber, with its different materials and structure, will have different sensitivity. By sensitivity, we mean the length scale over which the FOS strain is distributed when a sharp discontinuity occurs in the substrate, that is, the width of the measured strain peak when a crack occurs. Many applications of FOS either embed the fibers in a premade groove on reinforcing bars (Malek et al. 2019) or attach the fibers to the concrete surface (Brault and Hoult 2019a) to obtain the strain profile in reinforcement and concrete, respectively. In order to get accurate measurements of mechanical behavior in RC members, the implemented optical fibers need to be sensitive enough and, therefore, provide prominent peaks. In addition, they need to remain unbroken, with good durability, within the load level of interest. Regier and Hoult (2014) showed that fibers with a nylon coating and a polyimide coating were the most suitable options for strain measurements. A limited number of fibers are compatible with existing crack width calculation techniques. For example, the three methods developed by Brault and Hoult (2019a) require the peaks in the FOS strain profile to be very prominent; this eliminates the option to use many more stiff fibers, such as those with structured a polyamide (PA) outer sheath or stranded steel armored outer jacket, which are practically useful in relatively harsh civil engineering installation conditions.

To address these issues, a series of tests on six reinforced concrete specimens with different types of fiber-optic cables embedded in the reinforcing bars and concrete were conducted under uniaxial tension. Zhang et al. (2021) presented the influence of different fiber types on measurement capability when damage occurs and established a basic framework for optical fiber evaluation. In addition, to translate the spectral information into strain for customized optical fibers, two calibration methods were used. The first involved stretching fibers on a calibration rig, and the second involved a uniaxial tension test on bare rebar with optical fibers attached. The main objectives of this study were as follows:

1. Develop a deconvolution method that yields reliable estimates of crack widths, even for stiff fiber-optic cables, which tend to sustain measurement capability under higher damage levels but also have a reduced sensitivity to local concentrated strain caused by cracking.
2. Apply the aforementioned deconvolution method to optical fibers placed adjacent to the reinforcing bar–concrete interface to evaluate their capability in detecting distributed minor cracking.
3. Apply the proposed method to evaluate the variation in crack thickness through the thickness of the test specimen in order to help understand crack progression.
4. Measure bond-slip behavior using the optical fibers embedded in the reinforcing bars and evaluate it in comparison to existing bond-slip models.

Regarding the final objective, note that the bond of reinforcing bars is a key element for the ultimate load-carrying capacity of RC structures (Hong and Park 2012). However, many factors, including compressive concrete strength, concrete cover thickness, diameter of the reinforcing bars, stirrup area and spacing, and so forth, may affect local bond stress $\tau$, and there are large discrepancies in the existing bond stress–slip models in the literature (Wu and Zhao 2013). Most of these models were generated using strain measurements from strain gauges at several discrete points. For example, Hong and Park (2012) obtained the strain distribution curve by connecting neighboring points with a polynomial function; this technique may not be able to represent the actual local strain distribution.

## Experimental Setup

### Materials and Specimens

Six reinforced concrete specimens were tested under uniaxial tension. Fig. 1 is a schematic representation of the test setup. The length of the specimen in the longitudinal direction was 1,000 mm, and the height and width were both 120 mm. The Grade 60 No. 8 reinforcing bars used for the tests had a diameter of approximately 25.4 mm.

The six specimens (S1 to S6) were cast in two batches and left to harden for about 60 days before the tests. The two batches had the same mix design and were geometrically similar except for two premade grooves, 1.5 mm wide and 10 mm deep, placed midway along the length of the specimens in the second batch (S4, S5, S6), as shown in Fig. 1. To ensure a straight fiber shape after casting and, therefore, obtain accurate strain localization, all fibers were subjected to pretension by fixing the two ends, as shown in Fig. 2. For the first batch (S1, S2, S3), a mean compressive strength of 46 MPa was obtained by four concrete cylinder tests, and the mean elastic modulus was 25.3 GPa. For the second batch, the mean compressive strength was 40 MPa, and the mean elastic modulus was 27.0 GPa (Zhang et al. 2021). The concrete tensile strength of the current specimens was $f'_{ct} = 2$ MPa.

### Sensing Fibers

Seven different fiber-optic cables were used for the tests in order to investigate the effects of fiber type on crack detection. As seen in Fig. 3, a fiber-optic sensing cable contains three essential components: core, cladding, and coating. Details regarding the optical fibers used in the tests can be found in Table 1. All six specimens used the thinnest fiber (OFS_Y_02) to measure rebar deformation and two more fibers embedded in the concrete to detect internal damage. OFS_Y_02 had a polyimide coating. The OFS_Y_02 fiber had a low second moment of area and a relatively low bending strength, so it had to be installed with added precaution. The FOS installation process included the following steps: (1) cutting the two longitudinal ribs of the rebar using a band saw to create two notches to be the fiber pathways, which should be straight and flat to reduce noise; (2) cleaning the fiber pathways with water and industrial contact cleaner; and (3) bonding the FOS fiber to the bottom of the groove using a two-part adhesive, J-B Weld 50133 (J-B Weld, Sulphur Springs, Texas).

The FOS layout installed on the specimens is shown in Fig. 1. Three different types of fibers were placed at the same height as the center of the steel bar. In addition to the fibers embedded in the rebar, two fibers were installed in the concrete, and each of them went through two different locations. A1 and B1 represent two fiber sections placed 12 mm from the specimen surfaces labeled side A and side B in Fig. 1(b). To increase the accuracy of digital image correlation measurements, the two surfaces were covered with speckle patterns. A2 and B2 represent two fibers attached to the steel bar using zip ties. Table 2 shows the type of optical fibers at each location on the specimens.

An ODiSI 6100 sensor interrogator (Luna Innovations 2018) was used to take FOS measurements. For each test specimen, four channels were used to measure strain, each with a gauge length of

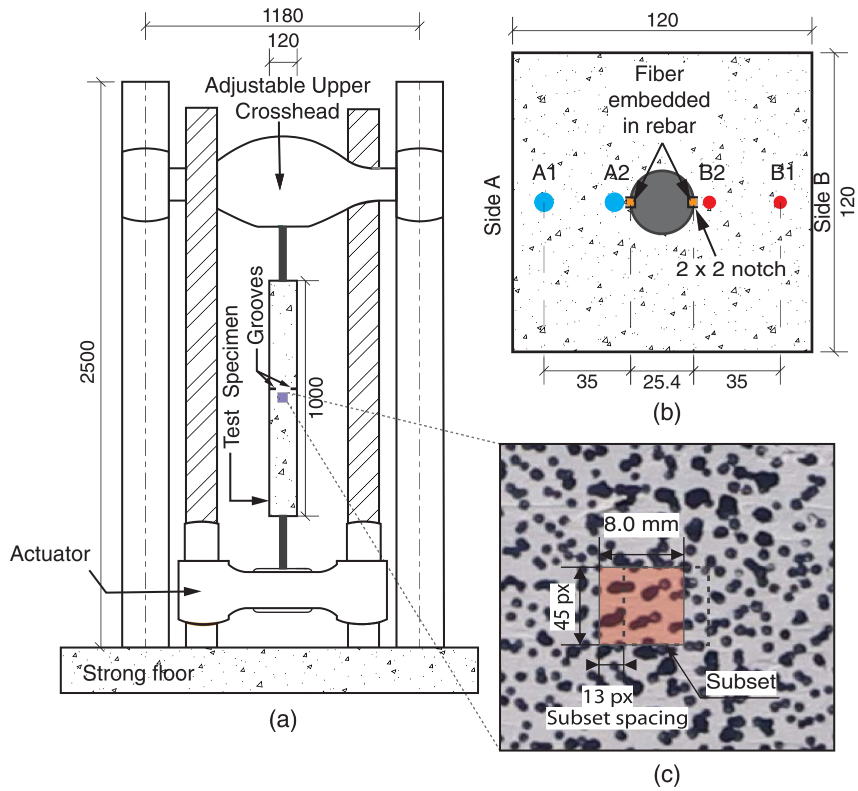


**Fig. 1.** Instrumentation setup: (a) force-controlled loading machine; (b) specimen cross section; and (c) speckle pattern for DIC processing. Dimensions are in millimeters; 1 mm = 0.0394 in.; and 1 kN = 0.225 kip.

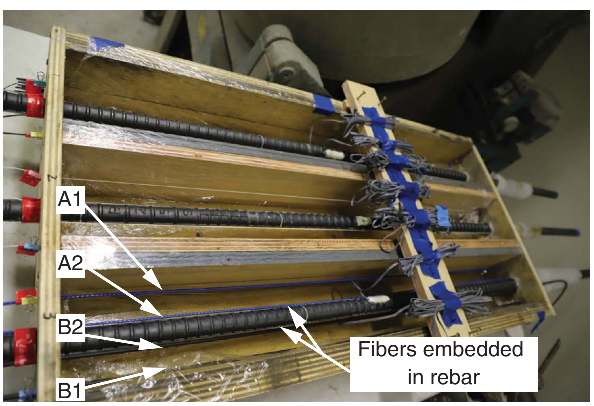


**Fig. 2.** Optical fibers subjected to pretension before casting.

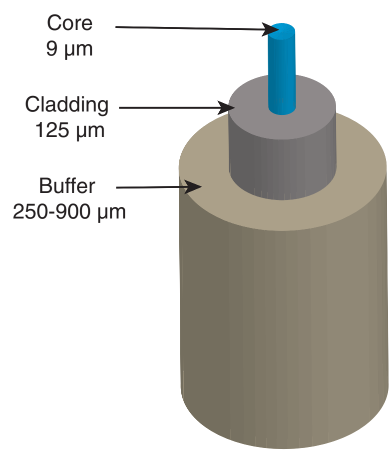


**Fig. 3.** Structure of the single-mode optical fiber.

1.3 mm. Because each load test lasted less than 2 h and the internal temperature of the laboratory was controlled, temperature fluctuations were negligible; therefore, they were not compensated for in strain measurements. For customized fibers, unique sensor reference files were created after calibration to compute strain. See Zhang et al. (2021) for the optical fiber calibration methods that were applied.

Fig. 4 shows an example strain measurement profile for A1 of S1, along with DIC results (see next subsection). Each crack in the concrete, which in theory would cause a sharp discontinuity in the strain, resulted in a distributed peak in the FOS readings. As was noted in the introduction, the width of the peak can be affected by debonding of the fiber from the concrete on either side of the crack, by deformation of the fiber coating, and by slip between the fiber layers. As a result, each type of optical fiber has a different peak width, which is referred to as the sensitivity of the optical fiber in this paper. Quantifying fiber sensitivity is essential for interpreting FOS strain results, as detailed in the section "Method for Correlating FOS Measurements and Crack Width."

### *Digital Image Correlation (DIC) Measurements*

The speckles on side A and side B were generated using a stamp roller from Correlated Solutions (Irmo, South Carolina) and consist of four important features: (1) high contrast, (2) consistent dot size (around 1.27 mm), (3) 30% coverage, and (4) randomness. The stamp had only about 10% coverage, so it was applied several times (3–4 times) for each patch, providing a random pattern [Fig. 1(c)].

**Table 1.** Tested optical fibers

| Acronym | Manufacturer | Color | Diameter (mm) | Jacket material | Standard |
|---|---|---|---|---|---|
| NZ_K_20 | Nanzee | Black | 2.0 | Central polyamide, polyurethane outer sheath | G.652.D |
| NZ_K_50 | Nanzee | Black | 5.0 | Stranded steel-armored outer jacket | G.652.D |
| NZ_W_09 | Nanzee | White | 0.9 | Polyamide | G.652.D |
| OFS_K_09 | OFS Optics | Black | 0.9 | Central silicone, PFA outer sheath | G.657.A1 |
| OFS_Y_02 | OFS Optics | Yellow | 0.155 | Polyimide | G.657.A1 |
| SLF_B_32 | Solifos AG | Blue | 3.2 | Central metal tube, structured PA outer sheath | N/A |
| TLC_W_09 | TLC | White | 0.9 | PVC | G.657 |

Source: Reproduced with permission from Zhang et al. (2021).
Note: N/A = not applicable.

**Table 2.** Optical fiber type embedded in each specimen

| Specimens | Side A | Side B | Rebar |
|---|---|---|---|
| S1 and S4 | NZ_K_20 | OFS_K_09 | OFS_Y_02 |
| S2 and S5 | NZ_W_09 | TLC_W_09 | OFS_Y_02 |
| S3 and S6 | SLF_B_32 | NZ_K_50 | OFS_Y_02 |

Digital images with widths of 6,240 pixels and heights of 4,160 pixels were captured using a Canon EOS 6D Mark II (Canon, Melville, New York) with an EF 24–105 mm IS STM lens (Canon) and then processed in Optecal version 2021, a two-dimensional (2D) DIC software package developed by Barthes (2021). Cracks were detected as concentrations of principal strain measured using DIC and as peaks in strain measurement along the optical fibers, as indicated in Fig. 4. DIC measurements correlated properly over the whole test campaign. The crack locations from FOS and DIC generally aligned well. For DIC, virtual extensometers were anchored on the two sides of each crack to calculate crack width and enable comparison with the crack widths calculated from FOS strain profiles, as discussed in subsequent sections.

### Load Test Setup and Procedure

The tests were performed at the structures laboratory of the Department of Civil and Environmental Engineering, University of California at Berkeley. The load frame is shown in Fig. 1. The loading machine was operated in force control, and the tension was applied to the rebar through ball hinges at the two ends. In this study, by following similar load protocols, it was expected that similar stress conditions and cracking behavior would be created in the specimens. The representative load histories for the two batches are shown in Fig. 5. There were seven load steps for each loading. The targeted load levels at the plateaus for the first batch (S1, S2, and S3) were 22.2, 44.5, 89.0, 89.0, 133.5, and 177.9 kN (5, 10, 20, 20, 30, and 40 kip) and then up until yielding. For the second batch, the targeted load levels at the plateaus were 22.2, 44.5, 89.0, 133.5, 177.9, and 222.4 kN (5, 10, 20, 30, 40, and 50 kip) and then up until yielding.

## Method for Correlating FOS Measurements and Crack Width

### FOS Measurements in Concrete

Fig. 6 shows specimen S2 after testing. Four distinct cracks occurred and were given alphanumeric designations (C1–C4) from bottom to top. Fig. 7 presents the fiber strain progression from 22.2 to 177.9 kN at locations A1 and B1 of each specimen. For S1, at 22.2 kN there were five strain peaks at approximately 0.21, 0.26, 0.44, 0.58, and 0.73 m for A1 but no obvious strain increases at 0.44 m for B1. The specimen was loaded further; at 89.0 kN, one more crack formed at 0.84 m. The amplitude of strain peaks increased linearly as the loads and crack widths increased. Optical fibers with different structures and coating/cladding materials provided significantly different strain readings under similar stress

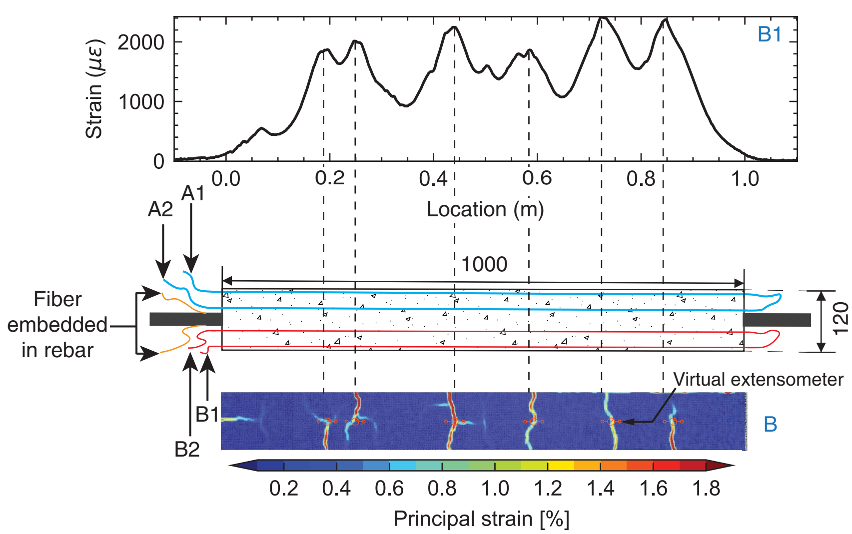


**Fig. 4.** Specimen plan view and postprocessed data of FOS_S1_B1 and DIC measurements (side B) along the length under a load of 177.9 kN (40 kip).

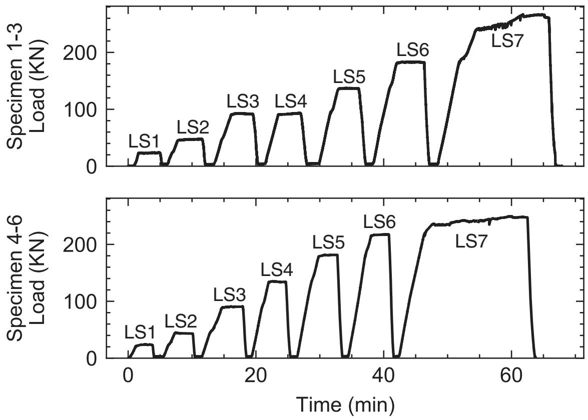


**Fig. 5.** Representation of the loading history.

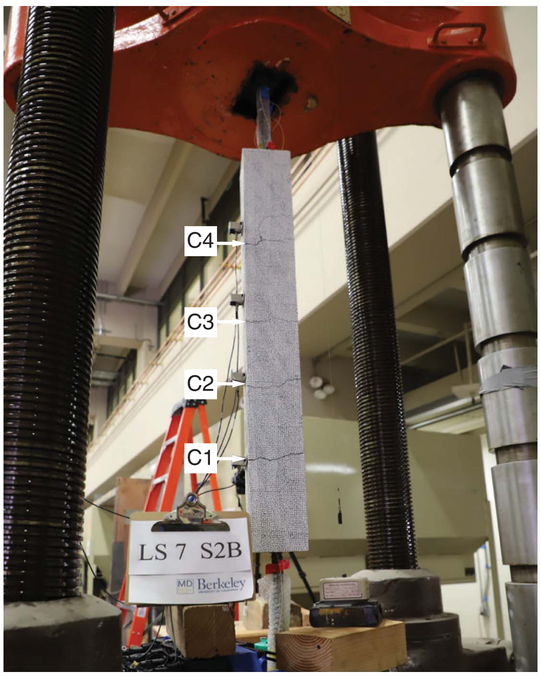


**Fig. 6.** S2 side B after testing, displaying the developed concrete cracks.

conditions. For example, the smoothness of the strain curves, the widths of strain peaks, and the loss of data reading capabilities under high loads varied considerably for the six types of fibers. At 177.9 kN, splitting cracks formed for all specimens, resulting in the emergence of additional small strain peaks (e.g., S2-A1/B1, S4-B1, and S5-A1) and the flattening of the strain measurement curves (e.g., S3-A1/B1 and S6-A1/B1). Detailed summaries of the progression of the strain distributions before and after yielding can be found in Zhang et al. (2021).

Fig. 7 also contains DIC strain fields for the last load step (177.9 kN). In general, the locations of fiber optic (FO) strain peaks corresponded well with the cracks visualized by the DIC principal tensile strain fields. NZ_W_09 was identified as the most sensitive optical fiber, with the most prominent peaks, while SLF_B_32 and NZ_K_50 were the two least sensitive optical fibers, with very wide peaks that merged into each other. However, all optical fibers detected the cracking to some degree. The following sections focus on the quantification of how FOS measurements correlated with crack opening and how fiber type affected this process.

### *Cracking Response of an RC Member Subjected to Uniaxial Tension*

Russo and Romano (1992) proposed a theory to predict the cracking response of a reinforced concrete member subjected to uniaxial tension. When cracking occurs, the member can exhibit equal concrete and steel strains in a central portion of the member [defined as a comparatively lightly loaded member (CLLM), see Fig. 8(a)] or exhibit a steel strain greater than the concrete strain at all locations along the member [defined as a comparatively heavily loaded member (CHLM), see Fig. 8(b)]. To correlate the FOS strain measurements with crack opening, it was necessary to subtract the distributed concrete strain from the strain profile measured with FOS to get the net strain caused by the cracks.

For a CLLM, the $x$-coordinate where the steel strain $\epsilon_S$ and concrete strain $\epsilon_C$ attain same value is defined as $X_R$, which is given by

$$X_R = \frac{1}{\delta}\left[\epsilon_{s0}\left(\frac{1}{2\gamma}\right)\right]^{2\delta/\beta} \tag{1a}$$

where

$$\beta = 1+\alpha, \quad \alpha \in (0.2\sim 0.45) \tag{1b}$$

$$\delta = \frac{1-\alpha}{2} \tag{1c}$$

$$\epsilon_{s0} = \frac{P}{E_s A_s} \tag{1d}$$

where $P$ = external force; and $E_s$ and $A_s$ = elastic modulus and sectional area of the steel bar, respectively

$$\gamma = \chi\frac{q_1}{\beta u_1^{\alpha}} \tag{1e}$$

where $q_1$ = maximum bond strength; and $u_1$ = minimum slip corresponding to $q_1$

$$\chi = \frac{(1+\xi)\Sigma_0}{A_s E_s} \tag{1f}$$

where $\Sigma_0$ = reinforcing bar circumference

$$\xi = \frac{n\rho}{\psi} = \frac{\frac{E_s}{E_c}\cdot\frac{A_s}{A_c}}{\psi} \tag{1g}$$

where $E_c$ and $A_c$ = elastic modulus and sectional area of the concrete, respectively; and

$$\psi = \frac{\int_{A_c}\sigma(x,r)dA_c}{A_c\sigma_c} \tag{1h}$$

where $\sigma_c$ = tensile concrete stress adjacent to the steel-concrete interface.

There are already reference values for centrally reinforced specimens. It is reasonable to assume $\psi = 0.75$ and $\alpha = 0.28$ (Russo and Romano 1992). The limit steel strain, which corresponds to the limit condition when both CLLM and CHLM behaviors occur and $X_R = 0.5L$, is given by

$$\epsilon_{s0l} = (2\gamma)^{1/2\delta}\left(\frac{l}{2}\delta\right)^{\beta/2\delta} \tag{2}$$

The steel strain at the loaded end where cracking occurs is given by

$$\epsilon_{s0\text{crack}} = \left(1+\frac{1}{\xi}\right)\epsilon_{ct} \tag{3}$$

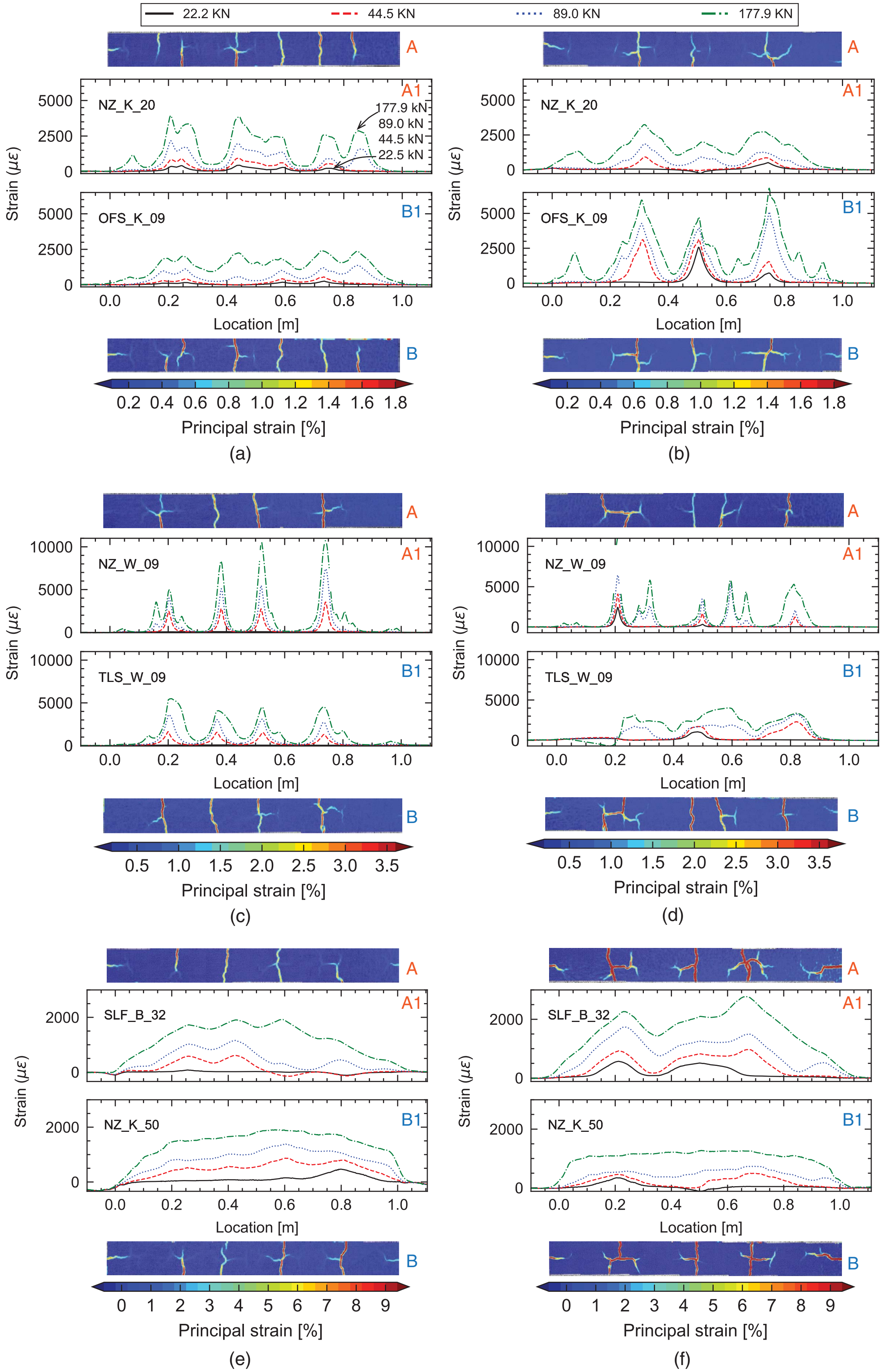

**Fig. 7.** Strain measurement with length along the six types of fibers for applied loads from 22.2 kN (5 kip) to 177.9 kN (40 kip). All DIC results are for 177.9 kN (40 kip).

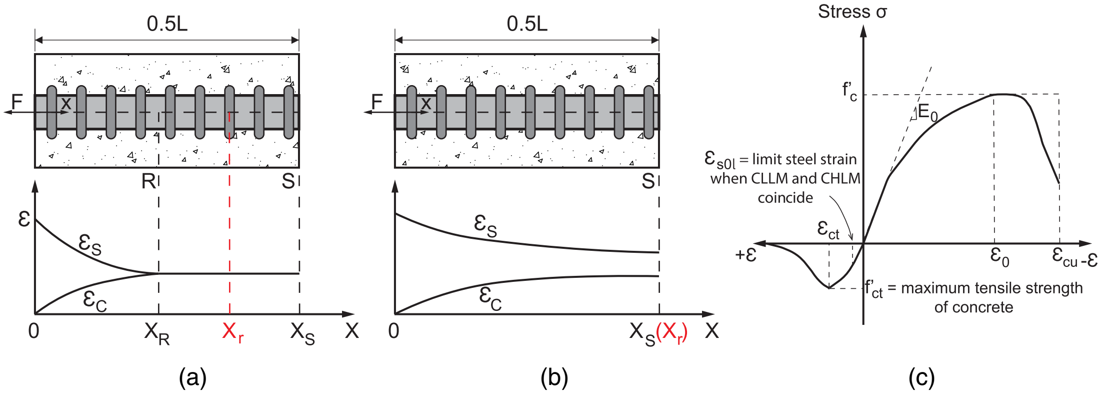


**Fig. 8.** Steel and concrete strain distributions in the RC members: (a) CLLM; (b) CHLM; and (c) uniaxial compressive and tensile stress-strain curve of concrete.

**Table 3.** Results of critical parameters for evaluating RC member cracking behavior

| Load (kN) | $\epsilon_{s0}$ ($\times 10^{-3}$) | $\epsilon_{s0l}$ ($\times 10^{-3}$) | $\epsilon_{s0\text{crack}}$ ($\times 10^{-3}$) | Model | $C$ ($\times 10^{-7}$) | $\epsilon_{c\max}$ ($\times 10^{-4}$) | $X_R$ (mm) |
|---|---|---|---|---|---|---|---|
| 22.2 | 0.22 | 2.78 | 0.29 | CLLM | N/A | 0.60 | 133.8 |
| 44.5 | 0.44 | | | CHLM | 0.00 | 1.20 | N/A |
| 89.0 | 0.87 | | | CHLM | 2.86 | 0.32 | N/A |
| 133.5 | 1.31 | | | CHLM | 7.63 | 0.21 | N/A |
| 177.9 | 1.75 | | | CHLM | 14.36 | 0.15 | N/A |
| 222.4 | 2.18 | | | CHLM | 22.81 | 0.12 | N/A |

where $\epsilon_{ct}$ = cracking strain at stress strength $f'_{ct}$. The maximum concrete strain at section $S$ is given by

$$\epsilon_{c\max} = \epsilon_{cR} = \frac{\xi}{1+\xi}\epsilon_{s0} \tag{4}$$

Table 3 shows the calculated results for the foregoing parameters. For the 22.2-kN load level, the CLLM solution is valid, because $\epsilon_{s0} \le \epsilon_{s0\text{crack}}$ and $\epsilon_{s0} \le \epsilon_{s0l}$. For load levels from 44.5 to 177.9 kN, CHLM behavior applies. This can also be verified by the approximation of concrete strain under different load levels. The concrete strain can be approximated by inverting the rebar strain measured by the optical fibers in the rebar groove as follows:

$$\epsilon_c(\epsilon_s) = \frac{V_r}{\epsilon_{s\max} - V_r}(\epsilon_{s\max} - \epsilon_s) \tag{5}$$

where $V_r$ = representative concrete strain from FOS readings in A1/B1 at a well-bonded section $X_r$. In the early stages, before the formation of large primary cracks, $V_r$ is expected to be close to the corresponding rebar strain. The expressions $\epsilon_s$ and $\epsilon_{s\max}$ represent the local and maximum FOS rebar strain measurements, respectively. For CLLM, $X_r$ can be taken as any random point within $X_R \sim X_s$, but for CHLM, it is essentially taken as $X_s$, as shown in Fig. 8. The importance of subtracting the approximate concrete strain $\epsilon_c$ [Eq. (5)] from the measured raw strain to measure crack magnitude depends on the loading level, as discussed in the following sections.

## *Optical Fiber Sensitivity*

In this section, a deconvolution method for correlating a measured distributed strain peak with crack opening is proposed. Only optical fibers embedded in the concrete at A1 and B1 were used to implement this deconvolution method because only primary cracks tend to propagate to the concrete surface and thereby contribute to the distributed peak in the FOS strain profile. The relatively large crack spacing and the crack localization allowed the cracks to be more accurately distinguished. (However, in the section "Crack Distribution Adjacent to Rebar," it is shown that this method can also be applied to the fibers at A2 and B2, where closely distributed internal cracks existed.) The method was evaluated through comparison with DIC virtual extensometer results.

To facilitate correlation, each FOS strain peak caused by a crack was fitted by a Lorentzian function of the form

$$L(x; x_0, \gamma, I) = I\left[\frac{\gamma^2}{(x-x_0)^2+\gamma^2}\right] \tag{6}$$

where $I$ = amplitude; $x_0$ = center; and $\gamma$ = parameter specifying the width. Fitting was achieved by a procedure specified subsequently in this section. Gaussian and Voigt functions were also trialed, but the Lorentzian function was selected because it provided the best fit of the FOS strain measurements.

Fig. 9 shows the measured strain in the rebar and the approximated concrete strain calculated from Eq. (5) for two load levels (28.1 and 31.4 kN). The figure also shows the measured FOS strain caused by the cracks alone (labeled "Crack strain profile"), which was calculated by subtracting the approximated concrete strain from the raw FOS strain measurement (i.e., FOS_S2_A1). Note that the crack strain profile was smoothed by curve fitting with nonlinear least-squares minimization using the LMFIT version 1.0.2 package:

$$\boldsymbol{w}^* = \arg\min_{\boldsymbol{w}} L(\boldsymbol{w}) \tag{7}$$

where

$$L(\boldsymbol{w}) = \frac{1}{n}\sum_{i}^{n}(y_i - \hat{y}_i)^2 \tag{8}$$

is the cost function; $n$ = number of data points; $y_i$ = predicted value; $\hat{y}_i$ = measured strain from FOS; and $\boldsymbol{w}$ = finite dimensional vector, the elements of which are parameters $I_i, \gamma_i, x_{0i}$, $i \in \{1, 2, \ldots, n\}$ in Eq. (6). Using mean square errors (MSE) as the cost function, we can find an approximate solution by minimizing the MSE [Eq. (7)]. Subsequently, the crack strain profile was decomposed into individual Lorentzian functions [Eq. (6)].

Crack locations were detected by peaks in the crack strain profile; these locations were then used as known centers of the decomposed functions. Fig. 9 also shows the Lorentzian fitting of each



J. Struct. Eng., 2021, 147(12): 04021212

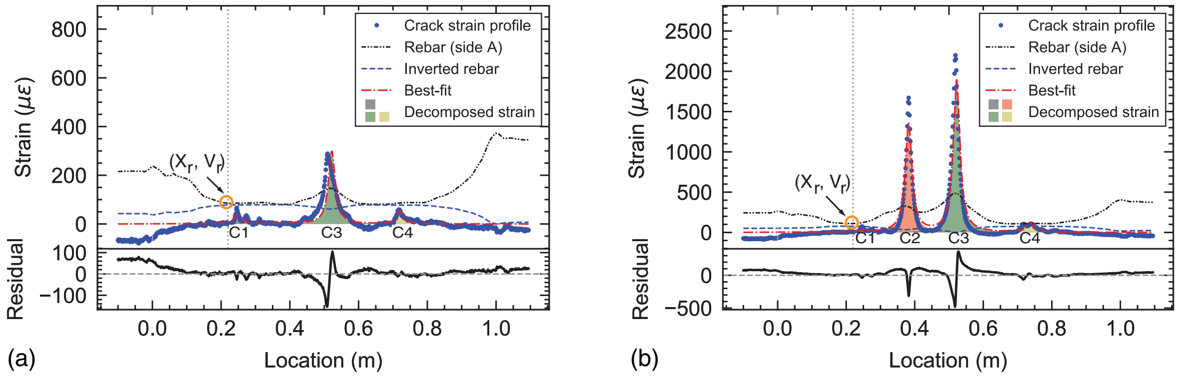


**Fig. 9.** Lower load level crack width calculation by subtracting inverted rebar strain from FOS_S2_A1: (a) 28.1 kN; and (b) 31.4 kN.

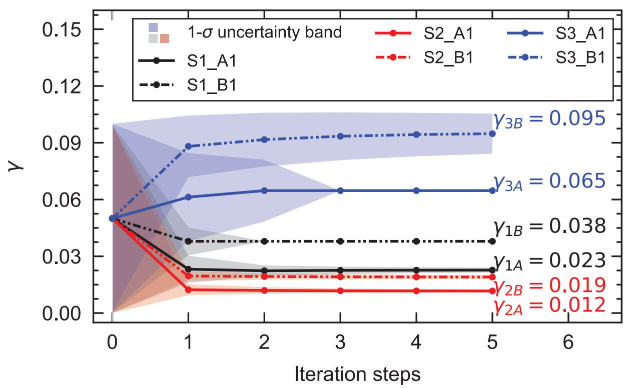


**Fig. 10.** Convergence of $\gamma$ in Lorentzian function.

crack and the summation of the Lorentzian distributions (labeled "best-fit"). The residual of the best fit and the crack strain profile are also depicted. Note that numerous cracks are fit in Fig. 9; only one main crack occurs in Fig. 9(a), while two main cracks occur in Fig. 9(b).

The results in Fig. 9(a) indicate that the approximate concrete strain [from Eq. (5)] was substantial at this load level, so it was necessary to deduct the approximated concrete strain from the raw FOS measurements to obtain a reliable crack width measurement; the specimen was in the CLLM category. Meanwhile, the concrete strain was negligible for specimen in CHLM [Fig. 9(b)], so the raw FOS measurements may have been sufficient for measuring crack width.

The parameter $\gamma$, which specifies the width of each Lorentzian function, is critical for evaluating a fiber's sensitivity, that is, the influence region of each crack. As external load increased, more cracks emerged and the magnitude ($I$) for each fitted Lorentzian distribution also increased. Meanwhile, $\gamma$ was found to remain approximately constant with increasing load for all fibers except for SLF_B_32 and NZ_K_50. For these two fibers, which were the most stiff and, therefore, yielded very wide peaks and flat distributions [Figs. 7(e and f)], the gamma parameter fluctuated more significantly.

To overcome this issue and find a representative $\gamma$ for each fiber across all load levels, an iterative method was adopted. An initial value of $\gamma_0 = 0.05$ was assigned with 0.05 variation. At each iteration step, the FOS strain measurements for each recorded time point were decomposed into Lorentzian functions. The mean of all $\gamma$ values was then used as the initial guess for the next iteration step, the standard deviation being the variation range. The results of the iteration are shown in Fig. 10, along with the uncertainty band. The uncertainty band width of optical fiber NZ_K_50 in S3_B1 and S6_B1 was large because its FOS strain readings were relatively flat; that is, this type of fiber was less sensitive, making peak decomposition less consistent. Nevertheless, after five steps, the converged $\gamma$, which essentially quantified the relative sensitivity, was selected to represent each optical fiber. The selection of a constant gamma for each cable over the entire loading range is discussed further in the section "Crack Width Measurements."

For each Lorentzian distribution [Eq. (6)], the area under the curve is equal to the crack width $W_{cr}$:

$$W_{cr} = \int_{-\infty}^{\infty} L(x)dx \approx \int_{x_0-3\gamma}^{x_0+3\gamma} I \cdot \frac{\gamma^2}{(x-x_0)^2+\gamma^2} dx = 2.5\gamma \cdot I \tag{9}$$

Fig. 11 shows the deconvolution of FOS strain measurements of six optical fibers at load step 6 (LS6) (177.9 kN) using the parameters generated from the iterative fitting. Generally, the deconvolution worked well. The application of a constant gamma for each fiber, provided by the iterative procedure, caused some reduction in fitting accuracy but yielded a reliable prediction of crack width measurement while mitigating the impact of multiple closely spaced cracks. However, splitting cracks that occurred at high loads were not directly considered and would increase the error in crack width prediction.

To provide a more direct measure of fiber sensitivity to local cracking, a sensitivity factor SF was defined as the ratio of the fitted amplitude to the corresponding crack width:

$$\mathrm{SF} = \frac{I}{W_{cr}} = \frac{1}{2.50\gamma} \tag{10}$$

The sensitivity factors for the six types of fibers are summarized in Table 4. Generally, the more stiff optical fibers (SLF_B_32 and NZ_K_50) provided lower resolution and had a lower sensitivity factor, while those with a higher sensitivity factor could provide higher resolution. NZ_W_09 in S2 had the highest SF.

## Results and Discussion

### Crack Width Measurements

To validate the feasibility of the aforementioned iterative method for strain distribution decomposition, DIC measurements on the specimen surface were compared with calculated crack widths using Eq. (9). The locations of fibers A1 and B1 were about 10 mm away from the closest DIC surface, so the crack widths were expected to

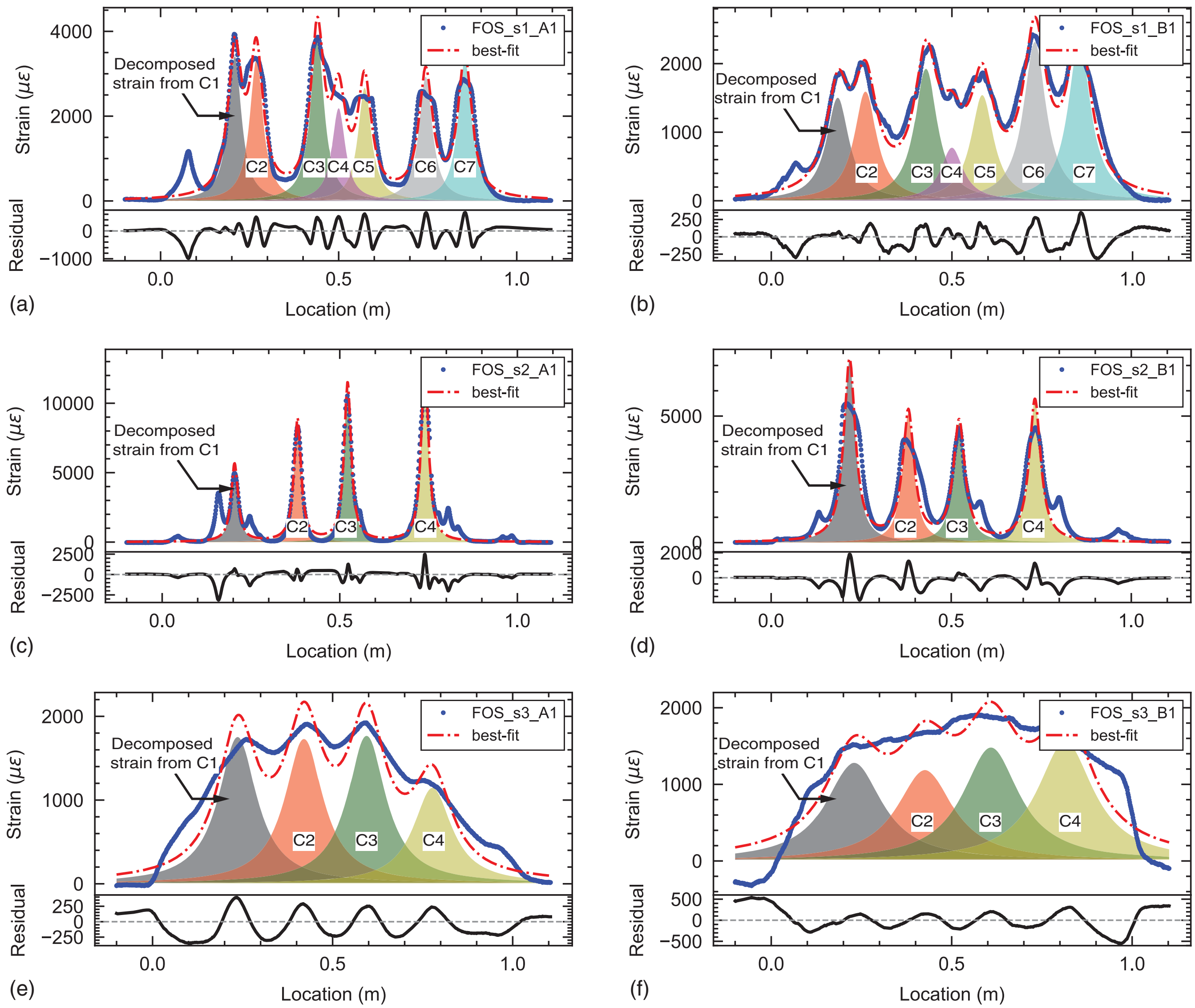


**Fig. 11.** Deconvolution of FO strain measurements under a load of 177.9 kN (40 kip) using parameters generated from iterative fitting: (a) S1 fiber A1 (NZ_K_20); (b) S1 fiber B1 (OFS_K_09); (c) S2 fiber A1 (NZ_W_09); (d) S2 fiber B1 (TLC_W_09); (e) S3 fiber A1 (SLF_B_32); and (f) S3 fiber B1 (NZ_K_50).

**Table 4.** Sensitivity factors from iterative method

| | Side A | | Side B | |
|---|---|---|---|---|
| Specimen | Fiber type | SF ($m^{-1}$) | Fiber type | SF ($m^{-1}$) |
| S1 | NZ_K_20 | 17.40 | OFS_K_09 | 10.53 |
| S2 | NZ_W_09 | 33.36 | TLS_W_09 | 21.07 |
| S3 | SLF_B_32 | 6.16 | NZ_K_50 | 4.21 |

be close but not necessarily identical. Fig. 12 shows the crack width deconvolution results using the raw FOS measured strain as well as the deconvolution results using the crack strain profile mentioned previously, in which the approximated concrete strain [Eq. (5)] is subtracted from the FOS measured strain to obtain the net strain. The displacement resolution of a typical DIC method is around ±0.1 to 0.01 pixels (Siebert et al. 2011). For the tested specimens, the mm/pixel ratio was around 0.18; therefore, the 0.005-mm DIC bias in Fig. 12 was acceptable. For the early stages of loading (up to about 30 kN), subtracting the concrete strain made a significant difference. After larger cracks emerged, the integrated crack width $W_{cr}$ from the net strain and the raw strain became approximately the same. Although it was challenging to quantify the improvement in accuracy provided by subtracting the concrete strain because of the limitation of the DIC resolution and the 10 mm distance between the DIC surface and the optical fibers, the adopted procedure provides a new method for measuring early stage minor cracking.

Fig. 13 shows the crack width of each individual crack in S2 from FOS measurements and DIC for each load step. In addition to the integrated crack width based on the representative $\gamma$ determined from the iterative fitting, Fig. 13 also shows the predicted crack width from free fitting, that is, the deconvolution results without confining $\gamma$. This free fitting was conducted for the following reasons. First, while the determination of a constant gamma was very useful in defining the sensitivity factor and comparing cables, it was not strictly necessary in order to allow the deconvolution. Second, one might hypothesize that gamma would increase with crack width due to continual debonding of the cable from the concrete; free fitting allowed this. An increase in gamma with crack width was not observed for the less stiff cables in S1 and S2, but an increase in gamma was observed for the two stiffer cables in S3.

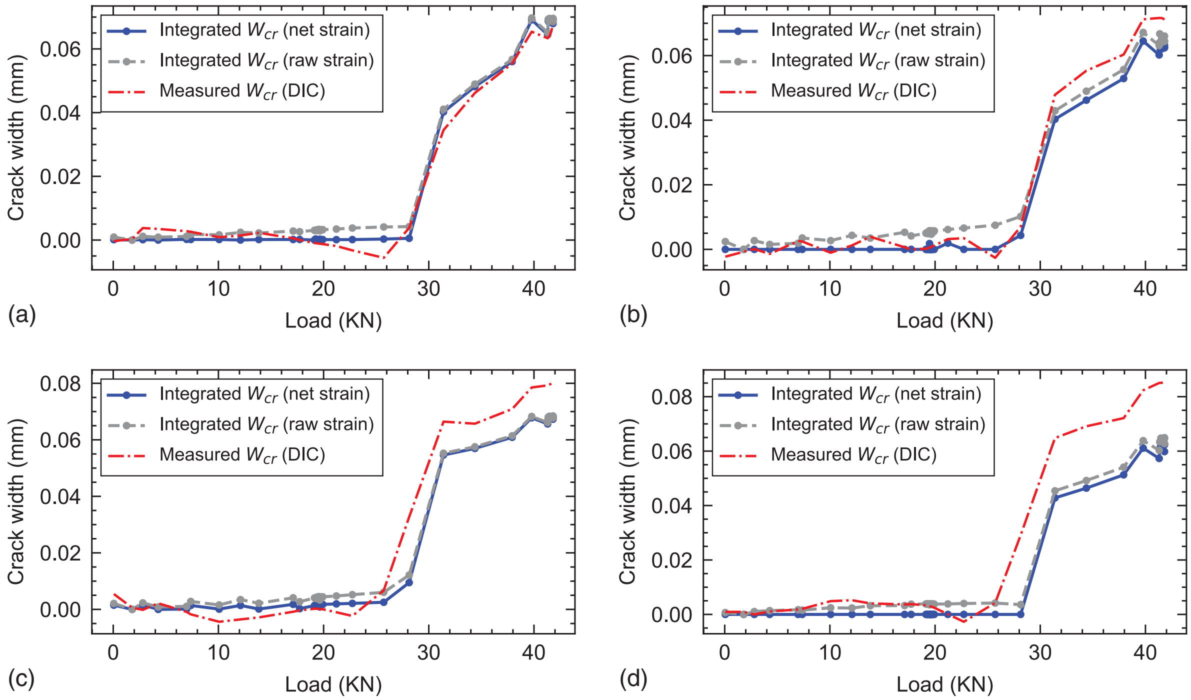


**Fig. 12.** Comparison between crack width from DIC with and without subtracting concrete strain: (a) S2 side A C2; (b) S2 side B C2; (c) S2 side A C3; and (d) S2 side B C3.

For the cables in S3, gamma could have been redefined as a function of crack width, but the free fitting results allowed this to happen naturally. Third, one might hypothesize that when secondary splitting cracks (i.e., the longitudinal cracks that branch off of the initial cracks) occurred at higher load levels, gamma would be affected; free fitting allowed gamma to change when these cracks occurred. It was difficult to determine exactly where splitting cracks occurred with respect to the fiber-optic cables, so eliminating cases of splitting cracks was not pursued.

Generally, the predicted crack width from both the fixed gamma and free fittings correlated reasonably well with DIC results. DIC measurements for crack width tended to be larger than crack width estimated by FOS across all load levels. Borosnyói and Snóbli (2010) presented experimental studies to investigate the variation in crack widths within the concrete cover of reinforced concrete tensile members. They confirmed that crack width increased through the concrete cover reasonably in the form of a power function, which explains why DIC (surface crack) results would be slightly larger than the FOS-generated crack width results.

The predicted crack width from both the fixed gamma and free fittings correlated very well over the lower load steps (LS1–4). However, at higher load levels (LS5–6), the free fitting predicted larger crack widths than were predicted in the fixed gamma case. This may have been due to the additional splitting cracks, although not all cases of load increase exhibited splitting cracks. Further, in some cases, the cracking situation is clearly more complex, and should not be expected to match. For example, crack S2-A-C1 was clearly an interaction of multiple cracks [Fig. 7(c)], so the free fitting artificially increased gamma and overpredicted the width of the main crack.

Figs. 21 and 22 in the Appendix summarize similar results for specimens S1 and S3, respectively, at six load steps. Both deconvolution methods generally provided reliable crack width predictions, even for the two most stiff and least sensitive fibers in S3, with a few notable exceptions. In some cases, the results should not be expected to match. For example, for crack S1-A-C3, crack propagation was complicated [Fig. 7(a)], and the DIC results were extremely prone to error near the crack tip/split. In other cases—for example, cracks S3-B-C3 and S3-B-C4 the primary crack was more obvious, but the splitting crack may have caused the constant gamma fitting to underpredict the results. The free fitting performed marginally better. Similar behavior was also observed in S2 for example, S2-B-C3 and S2-B-C4 (Fig. 13). For most other cases, the relative error for DIC and FOS crack width were within 10% during LS1–4. When one clean crack was observed, as for S1 cracks C5 and C6, both methods tended to perform better.

### *Crack Distribution Adjacent to Rebar*

Deconvolution of FOS measurements at A1 and B1 was relatively straightforward, because only primary cracks tend to propagate to the concrete surface. However, numerous internal cracks made it challenging to decompose the FOS strain profiles at locations A2 and B2 directly. Goto (1971) found that internal cone-shaped cracks were initiated at the steel bar ribs on either side of the primary cracks as shown in Fig. 14, but these internal cracks did not propagate to the surface. The rib spacing of the steel bar in the specimens was 16.4 mm. Therefore, using the representative $\gamma$ from the iterative fitting in Fig. 10, FOS measurements at A2 and B2 were decomposed into two categories: primary cracks and internal cracks, also known as Goto cracks.

In Fig. 15, the crack distribution along the length of S2, derived using deconvolution with the fixed gamma values resulting from the iterative fitting method, is presented. Strain peaks due to end effects were beyond the scope of this study and were not considered here. It is interesting to note that under 177.9 kN, internal cracks developed from the primary cracks at almost every rib and gradually decreased to zero at the well-bonded sections between the primary cracks. The locations of primary cracks on the two sides of S2 correlated accurately. However, the number of internal (Goto) cracks on side A was greater than the number on side B. This was likely

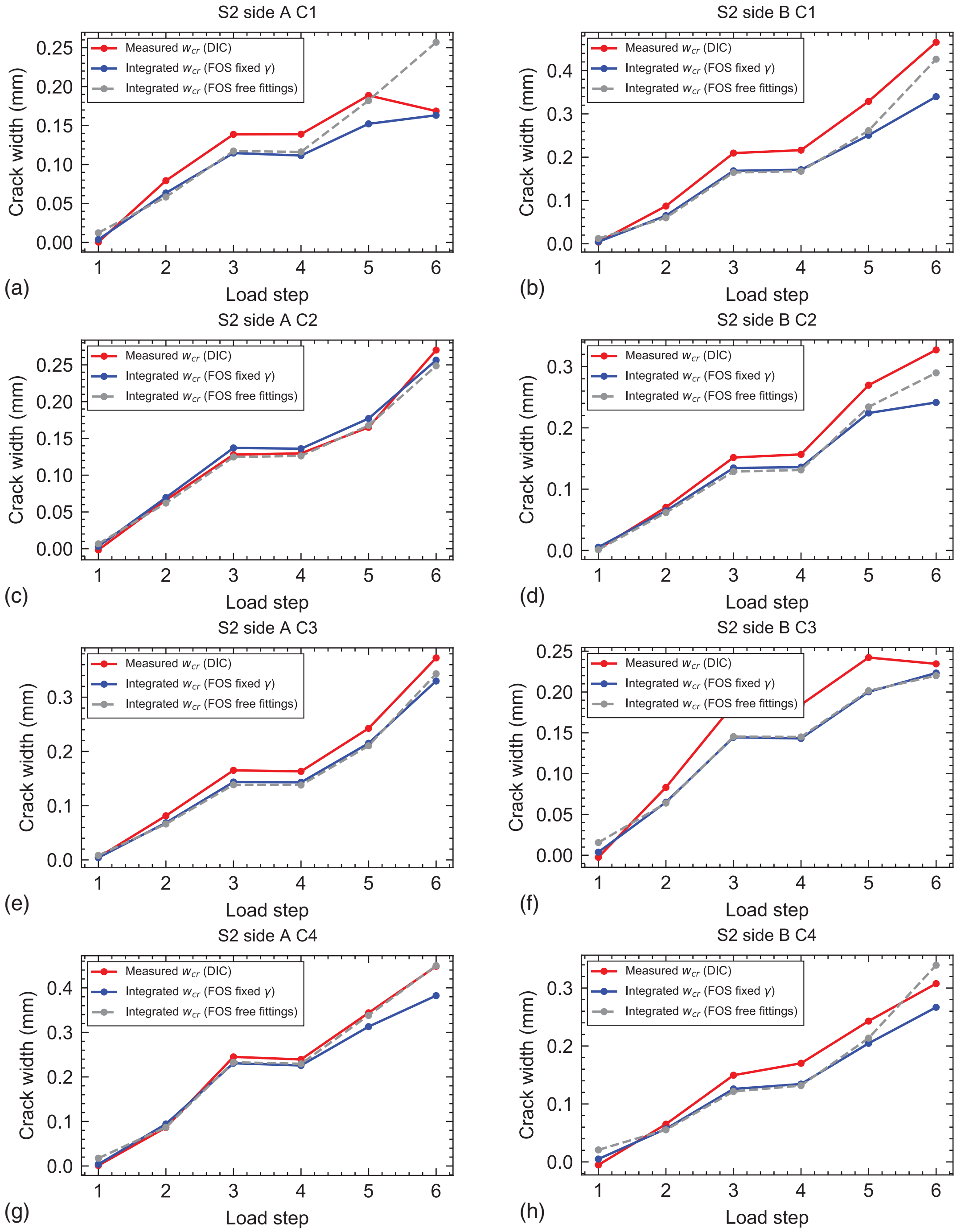


**Fig. 13.** Comparison between the crack width of S2 measured by DIC and calculated from the FOS measurements based on both free fitting and a fixed gamma value.

because the sensitivity factor for the optical fiber on side A was larger than the SF for the optical fiber on side B (Table 4), so internal cracks may have been smoothed together on side B. In addition, there may have been a slight difference in the internal crack distribution on either side of the specimen due to minor bending. Nevertheless, the proposed method of deconvolution provided detailed information of the internal damage to the RC member.

Fig. 16 shows the internal crack distribution at a lower load level of 44.5 kN. The internal cracks were significantly smaller than the primary cracks. After the formation of a primary crack, a further increase in stress in the rebar led to the initiation of internal cracks due to loss of adhesion (debonding) (Hornbostel and Geiker 2017). Compared with the results in Fig. 15, it is clear that as the load level increased, the internal cracks became wider. As the stress increased, internal cracks became secondary cracks, as demonstrated by distributions with multiple side peaks in Figs. 15(a and c).

## Fracture Surface

The four optical fibers lay in one plane along the centerline of each specimen. Therefore, using the calculated crack width from FOS and the DIC crack widths in the same plane as the fibers, the variation in crack width through the specimens could be obtained for

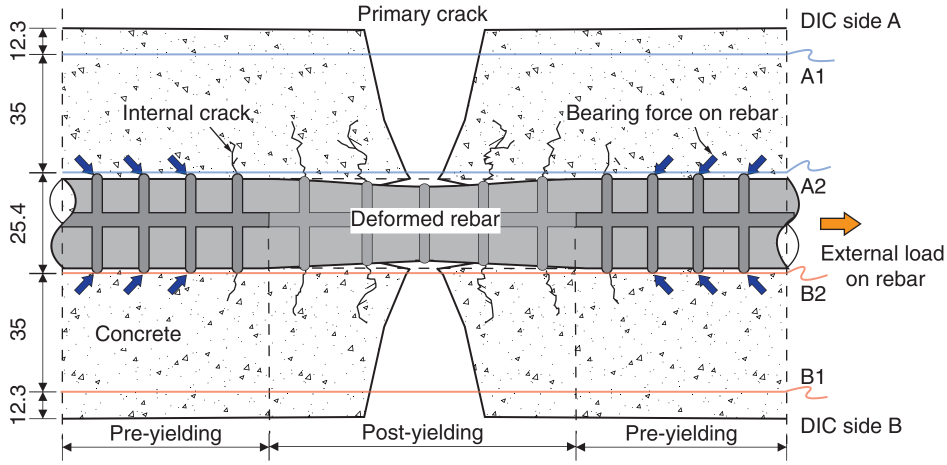


**Fig. 14.** Schematic illustration of internal damage cracking (millimeters).

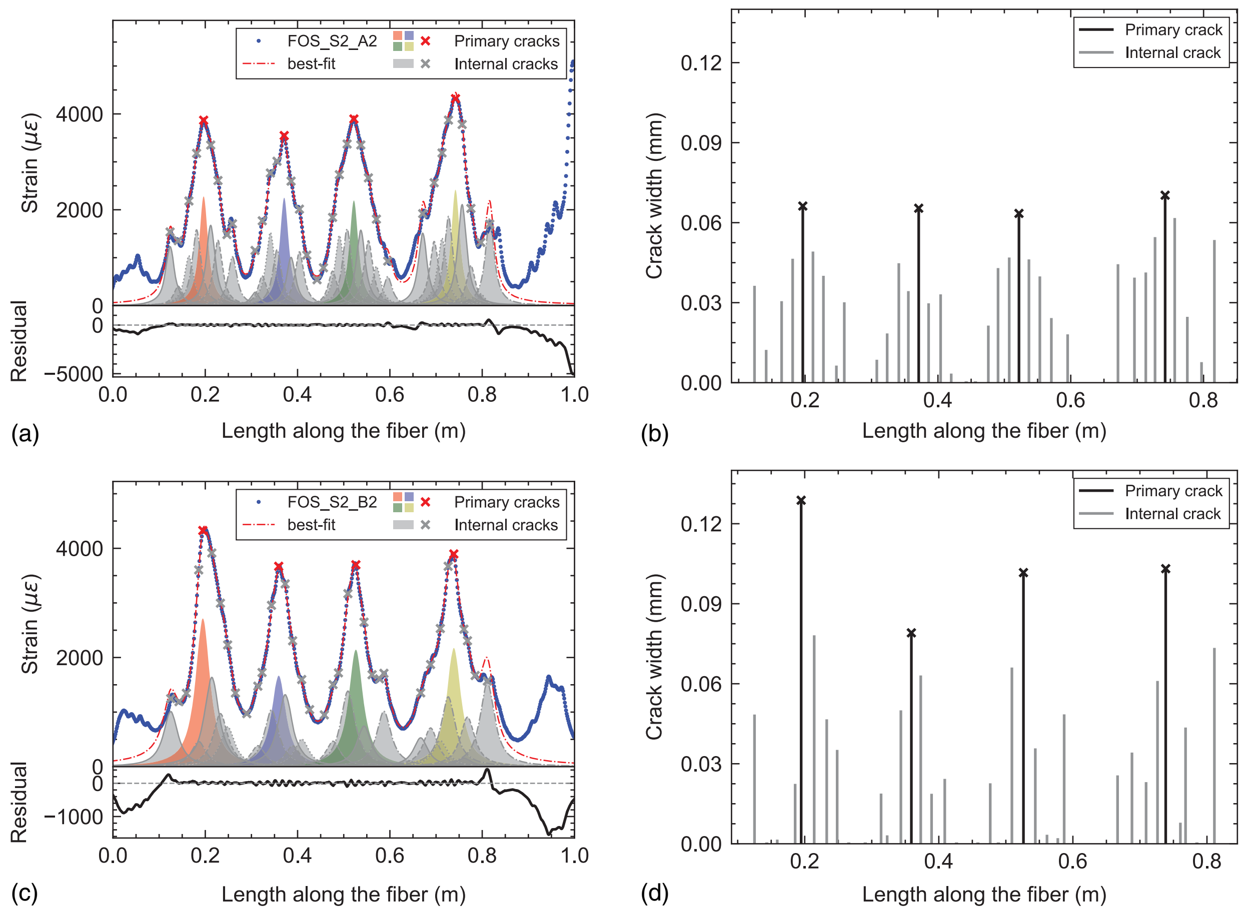


**Fig. 15.** Crack distribution along the specimen length under a load of 177.9 kN: (a) S2 A2 strain measurement deconvolution; (b) S2 A2 integrated width of primary and internal cracks; (c) S2 B2 strain measurement deconvolution; and (d) S2 B2 integrated width of primary and internal cracks.

each primary crack. Fig. 17(a) shows the variation of crack width along the line passing through all four optical fibers and two DIC surfaces. The figure confirms that the measured primary crack width decreased in the form of a power function from the concrete surface toward the reinforcing bar, as illustrated in Fig. 14. It also demonstrates that while the cracks were initiated at the surface of the reinforcing bar, they were often close to zero width near the steel–concrete interface (Borosnyói and Snóbli 2010). In Fig. 17(a), only the primary cracks were incorporated to get crack width at A2 and B2, while in Fig. 17(b), the primary crack widths and the adjacent internal crack widths between the valleys were integrated. Fig. 17(b) indicates a linear variation in crack width across the entire specimen, which could be evidence of bending that occurred along the length of the specimen. Fig. 17(c) is a schematic of a potential deformed shape that was deduced from the crack width distributions in Fig. 17(b).

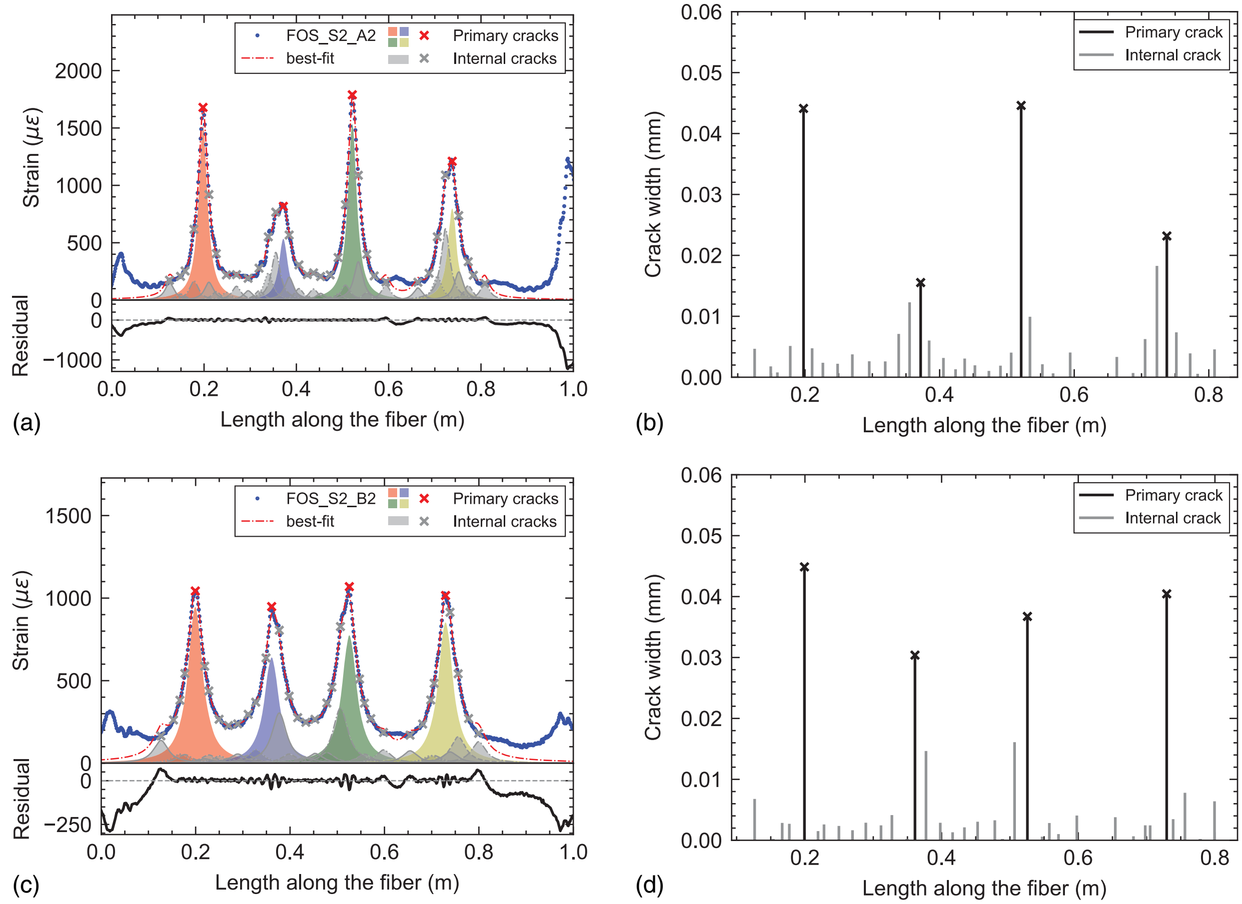


**Fig. 16.** Crack distribution along the specimen length under a load of 44.5 kN: (a) S2 A2 strain measurement deconvolution; (b) S2 A2 integrated width of primary and internal cracks; (c) S2 B2 strain measurement deconvolution; and (d) S2 B2 integrated width of primary and internal cracks.

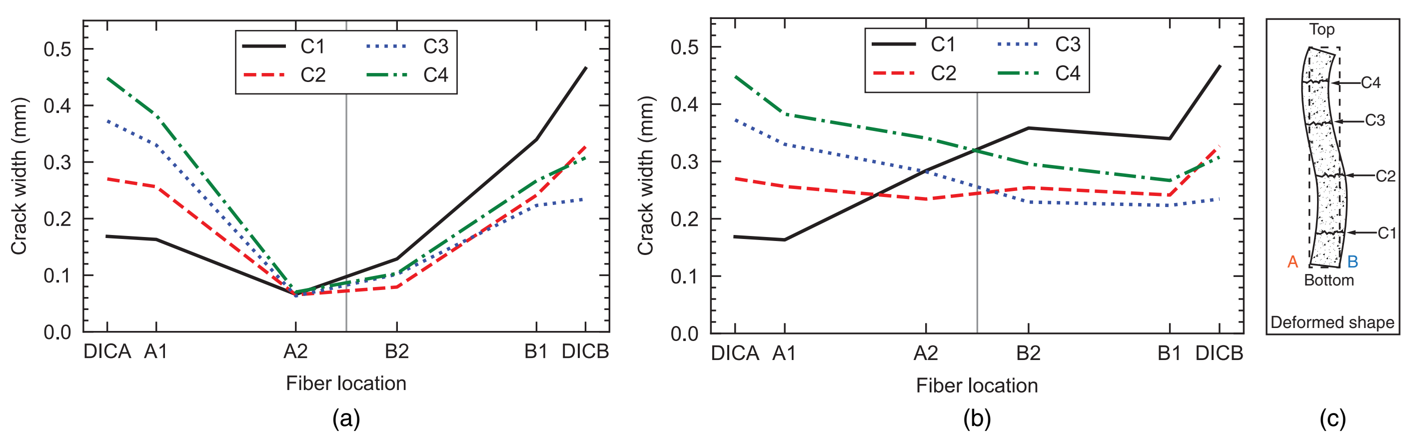


**Fig. 17.** Crack widths along the cross section for S2 under a load of 177.9 kN considering (a) only the primary cracks for A2 and B2; and (b) primary and internal cracks for A2 and B2; and (c) deformed shape of the specimen deduced from (b).

### *Bond Stress–Slip Relationship*

The last aspect investigated in this study was the feasibility of using FOS measurements to evaluate the bond stress–slip relationship. In addition, an innovative method of using FOS rebar strain to calculate crack width is proposed. The local slip $S$ between the concrete and rebar can be approximated as

$$S = \int (\epsilon_s(x) - \epsilon_c(x))dx' \qquad (11)$$

where $\epsilon_s$ = strain measurements from fibers embedded in the steel bar; and $\epsilon_c$ = approximate distributed concrete strain from Eq. (5).

In Fig. 18(a), the measured FOS reinforcement strain and the converted concrete strain from Eq. (5) in S2 side A under a load of 177.9 kN are presented. It is not useful to apply the proposed deconvolution method to fibers embedded in the reinforcement, because cracks do not pass through those optical fibers. In addition, as shown in Fig. 18(a), the strain in reinforcement had very small peak intervals; these were caused by transverse ribs instead of cracks.

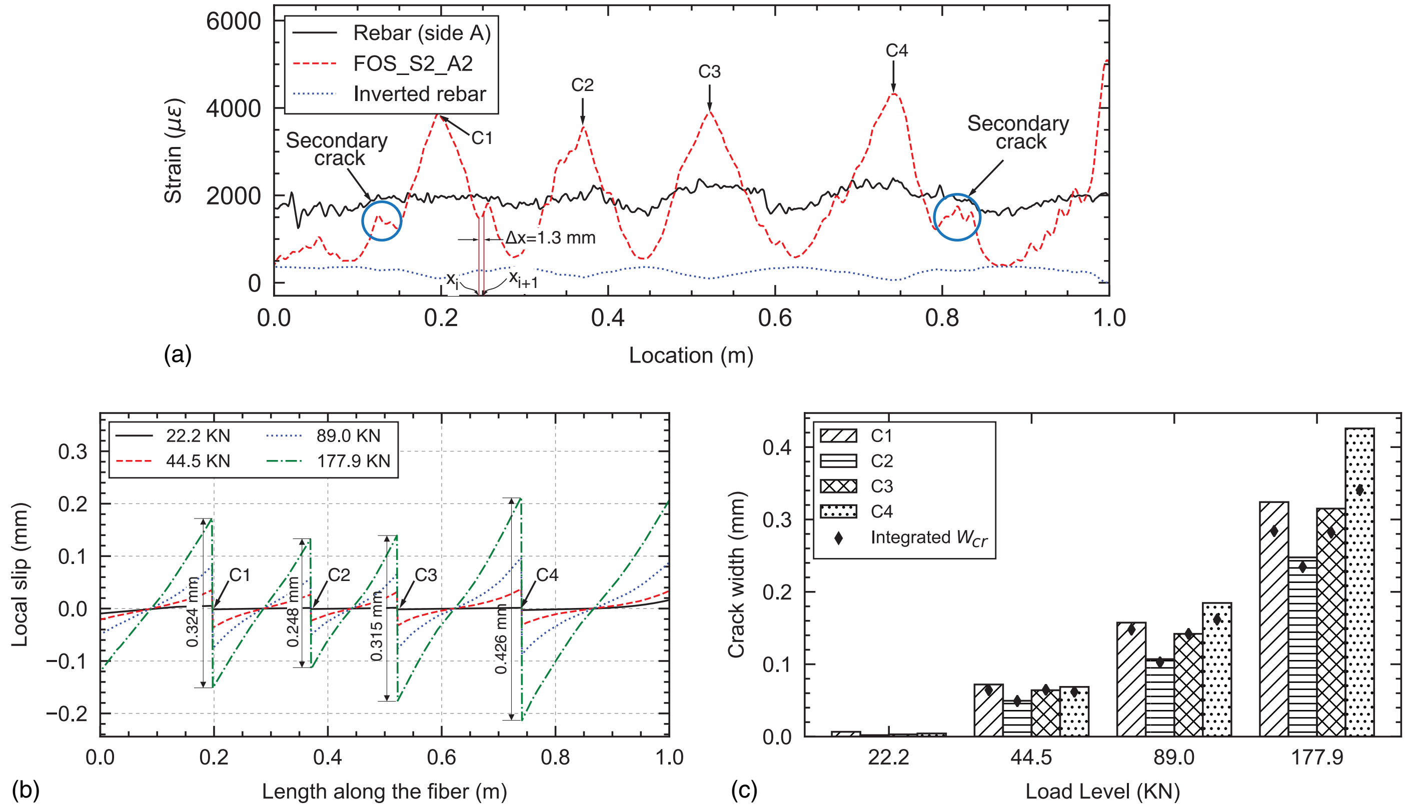


**Fig. 18.** Slip calculation in S2 side A: (a) FOS rebar strain and converted concrete strain under a load of 177.9 kN; (b) local slip (over 1.3 mm of subinterval gauge length) distributed along the specimen length; and (c) crack width from jump point in local slip for each primary crack.

At the valleys (i.e., at 0.10, 0.29, 0.44, 0.62, and 0.87 m), the concrete and steel bar were assumed to be well bonded. Hence, at those locations, the local slip defined by Eq. (11) was zero. Furthermore, the local slip at any point could be obtained by the integration of the strain from these valleys (i-1) with zero slip to the point concerned $i$ as

$$S_i(x) = S_{i-1}(x) + \int_{x_{i-1}}^{x_i} (\epsilon_s(x) - \epsilon_c(x))dx \tag{12}$$

Fig. 18(b) shows the calculated local slip under four different load steps. The slip difference on the left and right sides of each primary crack (C1–4) represented the total crack width between two adjacent valleys, including primary and internal cracks. The crack widths from jump points in the local slip are summarized in Fig. 18(c) and are also compared to the corresponding integrated crack widths obtained from FOS concrete strain measurements in Fig. 17(b). The crack width calculated using the two different methods agreed well at lower load levels. However, as the load level increased to 177.9 kN, a more significant difference was observed, especially for C1 and C4. This was likely caused by the shifting of actual locations with zero slip. As the reinforcement stress further increased under higher loads, slip tended to pass through the previously well-bonded sections, resulting in movement of these zero-slip locations. Therefore, the valleys in the FOS strain readings were not necessarily the actual locations with zero slip. In addition, the existence of internal minor cracks also affected the local slip within each section. Consequently, the proposed method for evaluating local slip lost its accuracy, and further refinement was required.

In order to get an accurate local slip calculation, it was assumed that each minor crack had the same effect on slip as the primary

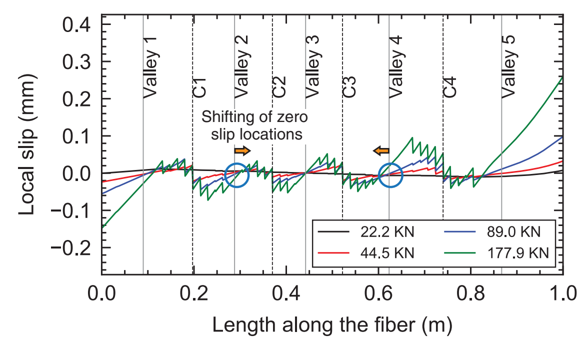


**Fig. 19.** Slip calculation after incorporating integrated minor and primary cracks from fitting method.

crack; that is, at the identified crack locations, there was a jump of slip that corresponded in magnitude to the under-curve area (AUC) of the fitted Lorentzian function. As shown in Fig. 19, the refined slip had a sawtooth distribution, and it always returned to a value close to zero at the valleys, which were the locations of local minima in the FOS strain measurements in the steel (which were the same locations in the FOS concrete strain measurements A2/B2 adjacent to the rebar). However, this also proved that the zero-slip segments shifted toward the center of the specimens under higher loads, causing considerable differences in FOS integrated crack widths and the ones from slip jump points, as observed in Fig. 18(c). The data at the first and last 0.1 m should not be considered, because only cracks in the range from 0.1–0.9 m were included. This gave us the distribution of local slip at a high resolution level and could be used to evaluate existing bond stress–slip models from a different perspective.



J. Struct. Eng., 2021, 147(12): 04021212

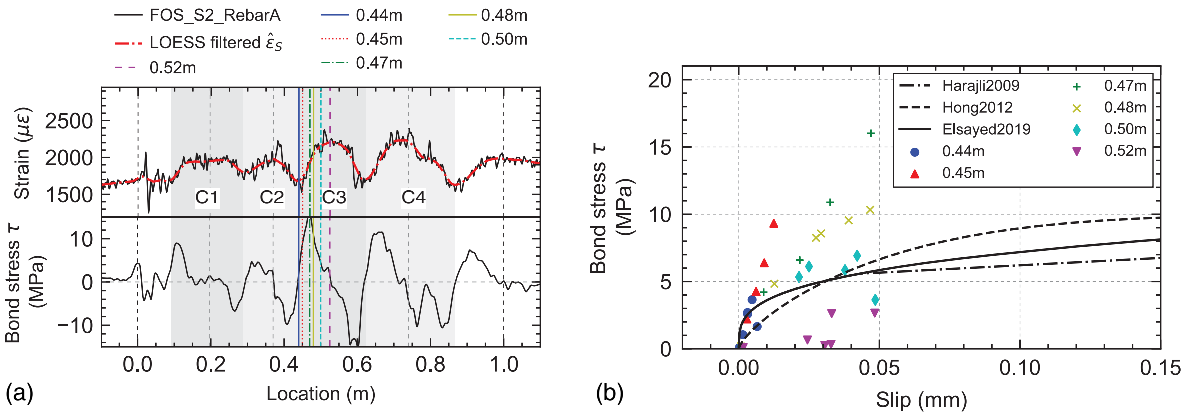


**Fig. 20.** (a) Bond stress from the derivative of smoothed FOS rebar strain measurements using LOESS filter in S2; and (b) experimental results of bond stress–slip relationship at a peak, a neighboring valley, and several intermediate points.

The bond stress between the rebar and concrete can be calculated by

$$\tau(x) = \frac{E_s d_s}{4} \cdot \frac{\partial \hat{\epsilon}_s(x)}{\partial x} \tag{13}$$

where $d_s$ and $E_s$ = diameter and elastic modulus of the rebar, respectively; and $\hat{\epsilon}_s(x)$ = distribution of the smoothed FOS rebar strain using a locally weighted scatterplot smoothing (LOESS) filter. For each data point within the selected window length, the LOESS filter applies a weighted linear regression and then replaces the data points with the corresponding value of the fitted polynomial. In general, the higher the window length, the smoother the filtered data will be and the more detailed information it will lose. Therefore, using the LOESS filter, the high local noise in the FOS reinforcement strain could be removed. Fig. 20(a) gives the filtered $\hat{\epsilon}_s(x)$ and its corresponding bond stress $\tau(x)$ using a LOESS filter with 5% window length. The figure shows that both the peaks and valleys in $\hat{\epsilon}_s(x)$ yield bond stresses were close to zero. Fig. 20(b) presents the bond stress–slip relationship at selected sections along S2, including the locations of the C3 peak, a neighboring valley, and four intermediate points in filtered $\hat{\epsilon}_s(x)$. At 0.44 m (valley point), local slip remained zero and the bond stress was also relatively small. However, near 0.52 m (peak), local slip attained high values, while bond stress stayed low. For the intermediate points from 0.47 to 0.50 m, there was a clear clockwise shifting of the bond stress–slip curve.

To interpret these bond-slip results, it is useful to compare them with existing bond-slip models. Eligehausen et al. (1983) reported the well-known Bertero-Eligehausen-Popov (BEP) model to investigate the local bond stress–slip relationships of deformed bars embedded in confined concrete for various bond conditions. Elsayed et al. (2019) derived a bond-slip law based on the BEP model that is mathematically expressed as follows:

$$\tau = \begin{cases} \tau_1 \left(\dfrac{s}{s_1}\right)^{\alpha} & \mathrm{s} \leq \mathrm{s}_1 \\ \tau_1 & \mathrm{s}_1 \leq \mathrm{s} < \mathrm{s}_2 \\ \tau_1 - \left(\dfrac{s_2 - s}{s_2 - s_3}\right)(\tau - \tau_3) & \mathrm{s}_2 \leq \mathrm{s} < \mathrm{s}_3 \\ \tau_3 & \mathrm{s} \geq \mathrm{s}_3 \end{cases} \tag{14}$$

where $\tau_1$ = maximum bond stress; $\alpha$ = curve-fitting parameter reflecting the degree of confinement; $s_1$ and $s_2$ = corresponding local bar slips at the beginning and end of the bond stress plateau, respectively; $s_3$ = rib spacing; and $\tau_3$ = residual bond stress. The aforementioned coefficients need calibration based on experimental results. However, due to the limit of the maximum loading during the tests, the maximum slip was only around 0.2 mm and we could not derive a complete bond stress–slip relationship based on the data. Nevertheless, the FOS measurements are still valuable for the validation of existing models at small slips. Harajli (2009) generated a four-stage bond stress–slip relationship of splitting failure for unconfined concrete. Considering the small slip in the specimen, we only needed to verify the first two stages: (1) an initial ascending part from zero bond stress up to $\alpha\tau_{sp}$, where $\alpha = 0.7$; this stage overlaps with the aforementioned BEP model for pull-out failure; and (2) a linearly increasing stage from $\alpha\tau_{sp}$ up to the splitting bond strength $\tau_{sp}$, which is defined by

$$\tau_{sp} = \gamma\sqrt{f'_c}\left(\frac{c + K_c}{d_s}\right)^{2/3} \tag{15}$$

where $\gamma = 0.78$ for unconfined normal strength concrete; $K_c$ = confinement parameters equals zero for plain concrete; and $c$ is the smaller of the side cover, bottom cover, or half the clear spacing between bars. The slip $s_{sp}$ at which the splitting bond strength $\tau_{sp}$ is attained is calculated as

$$s_{sp} = s_1 e^{3.3\ln(\tau_{sp}/\tau_1)} + s_0 \ln\left(\frac{\tau_1}{\tau_{sp}}\right) \tag{16}$$

where $s_0 = 0.15$ mm for unconfined concrete.

Murcia-Delso and Benson Shing (2015) proposed Eqs. (17) and (18) in the absence of experimental data:

$$\tau_1 = 1.163 f_c'^{0.75} \tag{17}$$

$$s_1 = 0.07 d_s \tag{18}$$

where $d_s$ = diameter of steel bar.

Hong and Park (2012) also proposed a bond model under axial tension as

$$\tau_b = k f_c'^{2/3}\left\{1 - \exp\left[-4500\left(\frac{S}{d_s}\right)^{1.45}\right]\right\}^{0.5} \times \exp\left[-5\left(\frac{S}{d_s}\right) + 5.5 f_R^{0.9}\right] \tag{19}$$

where $k$ = coefficient that accounts for the effects of the proposed model on bond stress, as defined in Eq. (20) for horizontally cast bar; and $f_R$ = relative rib area

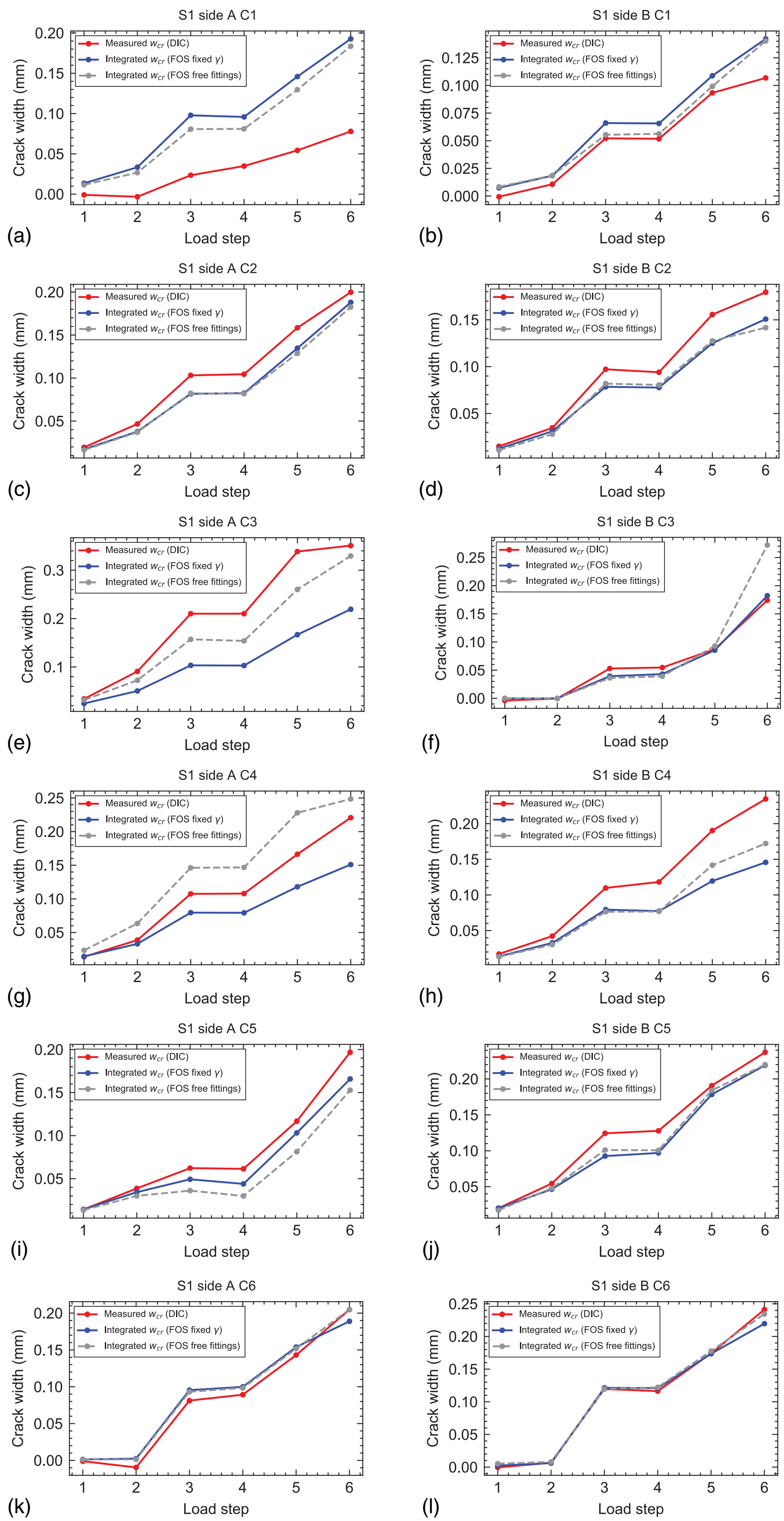


**Fig. 21.** Comparison between the crack width of S1 measured by DIC and calculated from DFOS measurements based on free fitting and iterative $\sigma$.

$$k = 0.2 \exp\left\{[-4.5 + 5.5 f_R]\right\} \frac{100}{A_c}\Big\} \tag{20}$$

$$f_R = \frac{A_R}{\pi d_s l_d} \tag{21}$$

where $l_d$ = rib spacing. This model was modified from Shima et al. (1987) and Ikki et al. (1996).

Fig. 20(b) also depicts the bond stress–slip relationship derived from the three models discussed in the foregoing: "Elsayed2019" [Eq. (14)], "Harajli2009" [Eqs. (15) and (16)] and "Hong2012" [Eqs. (19)–(21)]. Compared to the experimental data, the bond stress predicted by these models was either underestimated (0.44–0.50 m) or overestimated (0.52 m). Although the differences were largely related to different reinforcing bar properties, concrete properties, specimen dimensions, and local hardness of the concrete layer, it is clear that the measured bond stress–slip relationship also varied significantly depending on the investigated locations. The existing models failed to capture this location-dependent behavior during the early stages of loading, that is, for relatively small slip. For the model proposed by Elsayed et al. (2019), this was potentially because it was derived from pull-out tests, which have different stress distributions than the current uniaxial tension tests. They also assumed a linear distribution of reinforcement stress and a constant bond stress according to the strain readings at only three locations. Harajli's (2009) model was also derived using stresses and slip

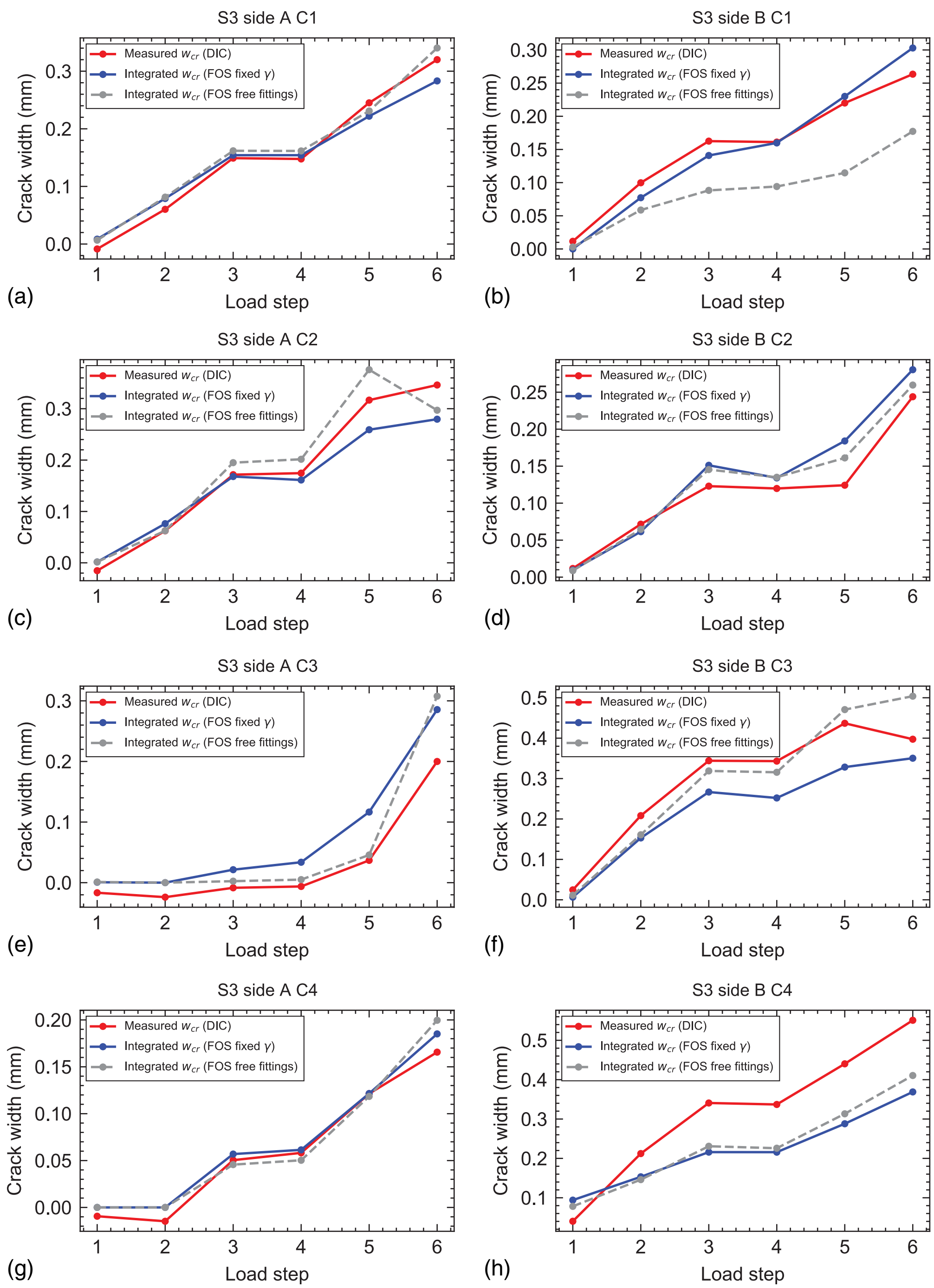


**Fig. 22.** Comparison between the crack width of S3 measured by DIC and calculated from DFOS measurements based on free fitting and iterative $\sigma$.

corresponding to average measurements. Moreover, Hong and Park (2012) tested RC members under axial tension loadings and claimed that the bond stress–slip relationship was the same independent of the locations along a specimen. However, they only installed a limited number of strain gauges and calculated slip based on integration of the fitted strain distribution; this ignored the possible slip compensation caused by minor cracking. In effect, the existing bond slip models provide an average of the very localized bond slip relationships measured along the length of the bar using fiber-optic cables.

## Conclusion

This paper considered damage detection in RC members using distributed fiber-optic sensors. Specifically, an investigation was performed on six reinforced concrete specimens under uniaxial tension to discover the effectiveness of using OFDR strain sensing to detect concrete cracking and damage at the interface between the concrete and reinforcing bars. The FOS system employed measured distributed strain at a spacing of 1.3 mm, providing detailed information of microcrack initiation and distribution, variation of crack widths within concrete cover, and local bond stress–slip behavior. From the investigations in this study, the major conclusions are as follows:

1. A deconvolution method for crack width measurements using FOS was proposed and evaluated against DIC measurements from six RC specimens tested in uniaxial tension. It was found that for both the more sensitive fiber-optic cables and the less sensitive ones that had better survivability, FOS measured crack widths with reliable accuracy throughout the loading of interest.
2. The deconvolution results provided detailed information about six types of fiber-optic cables, which enables their use for crack detection. In particular, the results indicated that stiff and less sensitive fibers still have potential for monitoring internal damage in infrastructure, but with the advantage of better durability to survive installation and the ability to maintain measurement capability at higher load levels.
3. The capability of FOS in detecting close minor cracks provided an alternative perspective of the distribution of internal cracks on either side of the primary cracks. It also clearly showed that the initiation and development of cracking in RC members could be measured up until load levels approaching failure.
4. The strain readings from the fiber-optic cables embedded in the steel bars and concrete demonstrated that the bond stress–slip relationship in RC structures is highly localized. The submillimeter resolution from OFDR meant that more detailed steel strain distributions and local slip could be obtained, and it revealed that the bond stress–slip relationship is location-dependent at early stages.

## Appendix. Graphs

Appendix contains Figs. 21 and 22.

## Data Availability Statement

Some or all data, models, or code generated or used during the study are available in a repository online in accordance with funder data retention policies (https://doi.org/10.6078/D1H422). Some or all data, models, or code that support the findings of this study are available from the corresponding author upon reasonable request.


## Acknowledgments

The authors gratefully acknowledge Cruz Carlos, Matthew Cataleta, and Phillip Wong for their technical support during preparation and testing of the specimens as well as their valuable assistance in optimizing the measurement systems.


## Notation

*The following symbols are used in this paper:*

$A_c$ = sectional area of concrete;
$A_R$ = projection area of a single rib on the cross section of a deformed bar;
$A_s$ = sectional area of steel bar;
$d_s$ = diameter of steel bar;
$E_c$ = elastic modulus of concrete;
$E_s$ = elastic modulus of steel bar;
$f'_{ct}$ = concrete tensile strength in the current specimens;
$f_R$ = relative rib area;
$I$ = amplitude of fitted Lorentzian function;
$l_d$ = rib spacing;
$P$ = external force;
$q_1$ = maximum bond strength;
SF = sensitivity factor of optical fibers;
$S_i$ = local slip at point $i$;
$u_1$ = minimum slip corresponding to $q_1$;
$W_{cr}$ = crack width;
$x_0$ = center of fitted Lorentzian function;
$\gamma$ = width parameter of fitted Lorentzian function;
$\epsilon_c$ = approximate distributed concrete strain;
$\epsilon_{c\max}$ = maximum concrete strain at section $S$;
$\epsilon_{ct}$ = cracking strain at stress strength $f'_{ct}$;
$\epsilon_s$ = strain measurements from fibers embedded in the steel bar;
$\epsilon_{s0\mathrm{crack}}$ = steel strain at the loaded end, where cracking occurs;
$\epsilon_{s0l}$ = limit steel strain;
$\Sigma_0$ = reinforcing bar circumference; and
$\sigma_c$ = tensile concrete stress adjacent to the steel–concrete interface.

## References


Barrias, A., J. R. Casas, and S. Villalba. 2016. "A review of distributed optical fiber sensors for civil engineering applications." *Sensors* 16 (5): 748. https://doi.org/10.3390/s16050748.

Barrias, A., J. R. Casas, and S. Villalba. 2018. "Embedded distributed optical fiber sensors in reinforced concrete structures—A case study." *Sensors* 18 (4): 980. https://doi.org/10.3390/s18040980.

Barthes, C. 2021. "Optecal." Accessed April 21, 2021. https://optecal.com/.

Borosnyói, A., and I. Snóbli. 2010. "Crack width variation within the concrete cover of reinforced concrete members." *Építõanyag* 62 (3): 70–74. https://doi.org/10.14382/epitoanyag-jsbcm.2010.14.

Brault, A., and N. Hoult. 2019a. "Monitoring reinforced concrete serviceability performance using fiber-optic sensors." *ACI Struct. J.* 116 (1): 57–70. https://doi.org/10.14359/51710870.

Brault, A., and N. A. Hoult. 2019b. "Distributed reinforcement strains: Measurement and application." *ACI Struct. J.* 116 (4): 115–127. https://doi.org/10.14359/51714483.

Brault, A., N. A. Hoult, T. Greenough, and I. Trudeau. 2019. "Monitoring of beams in an RC building during a load test using distributed sensors." *J. Perform. Constr. Facil.* 33 (1): 04018096. https://doi.org/10.1061/(ASCE)CF.1943-5509.0001250.

Davis, M. B., N. A. Hoult, S. Bajaj, and E. C. Bentz. 2017. "Distributed sensing for shrinkage and tension stiffening measurement." *ACI Struct. J.* 114 (3): 753–764. https://doi.org/10.14359/51689463.

Eligehausen, R., E. P. Popov, and V. V. Bertero. 1983. *Local bond stress-slip relationships of deformed bars under generalized excitations*. Rep. No. UCB/EERC 83-23. Berkeley, CA: Univ. of California.

Elsayed, M., M. L. Nehdi, and F. Ghrib. 2019. "Predicting behavior of grouted dowel connections using interfacial cohesive elements." *Appl. Sci.* 9 (11): 2344. https://doi.org/10.3390/app9112344.

Goto, Y. 1971. "Cracks formed in concrete around deformed tension bars." *J. Am Concr. Inst. Proc.* 68: 244–251. https://doi.org/10.14359/11325.

Haefliger, S., J. Mata-Falcón, and W. Kaufmann. 2017. "Application of distributed optical measurements to structural concrete experiments." In *Proc., 4th Conf. on Smart Monitoring, Assessment and Rehabilitation of Civil Structures*, 159. Paris: International Union of Laboratories and Experts in Construction Materials, Systems and Structures.

Harajli, M. 2009. "Bond stress–slip model for steel bars in unconfined or steel, FRC, or FRP confined concrete under cyclic loading." *J. Struct. Eng.* 135 (5): 509–518. https://doi.org/10.1061/(ASCE)0733-9445(2009)135:5(509).

Hong, S., and S.-K. Park. 2012. "Uniaxial bond stress-slip relationship of reinforcing bars in concrete." *Adv. Mater. Sci. Eng.* 2012: 1–12. https://doi.org/10.1155/2012/328570.

Hornbostel, K., and M. Geiker. 2017. "Influence of cracking on reinforcement corrosion." In *Crack width calculations methods for large concrete structures*. Oslo, Norway: Nordic Concrete Federation.

Ikki, N., O. Kiyomiya, and M. Yamada. 1996. "Experimental study on the effects of numerous factors on bond-slip relationship." *Doboku Gakkai Ronbunshu* 1996 (550): 73–83. https://doi.org/10.2208/jscej.1996.550_73.

Luna Innovations. 2018. *Optical distributed sensor interrogator model ODiSI 6100: User's guide*. Blacksburg, VA: Luna Innovations.

Malek, A., A. Scott, S. Pampanin, and N. A. Hoult. 2019. "Postyield bond deterioration and damage assessment of rc beams using distributed fiber-optic strain sensing system." *J. Struct. Eng.* 145 (4): 04019007. https://doi.org/10.1061/(ASCE)ST.1943-541X.0002286.

Mata-Falcón, J., S. Haefliger, M. Lee, T. Galkovski, and N. Gehri. 2020. "Combined application of distributed fibre optical and digital image correlation measurements to structural concrete experiments." *Eng. Struct.* 225 (Dec): 111309. https://doi.org/10.1016/j.engstruct.2020.111309.

Murcia-Delso, J., and P. Benson Shing. 2015. "Bond-slip model for detailed finite-element analysis of reinforced concrete structures." *J. Struct. Eng.* 141 (4): 04014125. https://doi.org/10.1061/(ASCE)ST.1943-541X.0001070.

Poldon, J. J., N. A. Hoult, and E. C. Bentz. 2019. "Distributed sensing in large reinforced concrete shear test." *ACI Struct. J.* 116 (5): 235–245. https://doi.org/10.14359/51716765.

Regier, R., and N. A. Hoult. 2014. "Distributed strain behavior of a reinforced concrete bridge: Case study." *J. Bridge Eng.* 19 (12): 05014007. https://doi.org/10.1061/(ASCE)BE.1943-5592.0000637.

Rodríguez, G., J. R. Casas, and S. Villaba. 2015. "Cracking assessment in concrete structures by distributed optical fiber." *Smart Mater. Struct.* 24 (3): 035005. https://doi.org/10.1088/0964-1726/24/3/035005.

Russo, G., and F. Romano. 1992. "Cracking response of rc members subjected to uniaxial tension." *J. Struct. Eng.* 118 (5): 1172–1190. https://doi.org/10.1061/(ASCE)0733-9445(1992)118:5(1172).

Shima, H., L.-L. Chou, and H. Okamura. 1987. "Micro and macro models for bond in reinforced concrete." *J. Fac. Eng.* 39 (2): 133–194.

Siebert, T., H.-R. Schubach, and K. Splitthof. 2011. "Recent developments and applications for optical full field strain measurement using ESPI and DIC." In Vol. 7997 of *Proc., 4th Int. Seminar on Modern Cutting and Measuring Engineering*. Bellingham, WA: International Society for Optics and Photonics.

Villalba, S., and J. R. Casas. 2013. "Application of optical fiber distributed sensing to health monitoring of concrete structures." *Mech. Syst. Sig. Process.* 39 (1–2): 441–451. https://doi.org/10.1016/j.ymssp.2012.01.027.

Wu, Y.-F., and X.-M. Zhao. 2013. "Unified bond stress–slip model for reinforced concrete." *J. Struct. Eng.* 139 (11): 1951–1962. https://doi.org/10.1061/(ASCE)ST.1943-541X.0000747.

Zhang, S., H. Liu, A. A. S. Coulibaly, and M. DeJong. 2021. "Fiber optic sensing of concrete cracking and rebar deformation using several types of cable." *Struct. Control Health Monit.* 28 (2): e2664. https://doi.org/10.1002/stc.2664.